Spatio-temporal variations of HNO₃ total column from 9 years of IASI measurements - A driver study

Gaétane Ronsmans[1], Catherine Wespes[1], Daniel Hurtmans[1], Cathy Clerbaux[1,2], and
Pierre-François Coheur[1]

[1]Université Libre de Bruxelles (ULB), Faculté des Sciences, Chimie Quantique et Photophysique, Brussels, Belgium
[2]LATMOS/IPSL, UPMC Univ. Paris 06 Sorbonne Universités, UVSQ, CNRS, Paris, France

Correspondence to: Gaétane Ronsmans (gronsman@ulb.ac.be)

Abstract. This study aims at understanding the spatial and temporal variability of HNO₃ total columns in terms of explanatory variables. To achieve this, multiple linear regressions are used to fit satellite-derived time series of HNO₃ daily averaged total columns. First, an analysis of the IASI 9-year time series (2008-2016) is conducted based on various equivalent latitude bands. The strong and systematic denitrification of the southern polar stratosphere is observed very clearly. It is also possible

5 to distinguish, within the polar vortex, three regions wich are differently affected by the denitrification. Three exceptional denitrification episodes in 2011, 2014 and 2016 are also observed in the northern hemisphere, due to unusually low arctic temperatures. The time series are then fitted by multivariate regressions to identify what variables are responsible for HNO₃ variability in global distributions and time series, and to quantify their respective influence. Out of an ensemble of proxies (annual cycle, solar flux, quasi-biennial oscillation, multivariate ENSO index, Arctic and Antarctic oscillations and volume of

10 polar stratospheric clouds), only the ones defined as significant (p-value < 0.05) by a selection algorithm are retained for each equivalent latitude band. Overall, the regression gives a good representation of HNO₃ variability, with especially good results at high latitudes (60-80% of the observed variability explained by the model). The regressions show everywhere the dominance of the annual variability, which is related to specific chemistry and dynamic depending on the latitudes. We find that the PSCs also have a major influence in the polar regions, and that their inclusion in the model improves the correlation coefficients and

15 the residuals. However, there is still a relatively large part of the HNO₃ variability that remains unexplained by the model, especially in the intertropical regions, where factors not included in the regression model (such as vegetation fires or lightning) may be at play.

1   Introduction

Nitric acid (HNO₃) is known to influence the ozone (O₃) concentrations in the polar regions, because of its role of NOₓ

20 ($\equiv$ NO+NO₂) reservoir and its ability to form polar stratospheric clouds (PSCs) inside the vortex (Solomon, 1999; Urban et al., 2009; Popp et al., 2009). In the stratosphere, HNO₃ forms from the reaction between OH and NO₂ (produced by the reaction N₂O+O¹D) and is destroyed by its reaction with OH or its photodissocation, both of these reactions being slow in daytime and virtually inexsitent during nighttime (McDonald et al., 2000; Santee et al., 2004). This leads to photochemical lifetimes be-

tween 1 and 3 months up to 30 km altitude and around 10 days above (Austin et al., 1986), inducing similar transport pathways for O_3 and NO_y (the sum of all reactive nitrogen species, i.e. including HNO_3) in general (Fischer et al., 1997). During the polar winter, with the arrival of low temperatures, polar stratospheric clouds (PSCs), composed of HNO_3, sulphuric acid (H_2SO_4) and water ice (H_2O) form within the vortex (Voigt et al., 2000; von König et al., 2002). They act as sites for heterogeneous

5   reactions, turning inactive forms of chlorine and bromine into active radicals, and leading to the depletion of O_3 in the polar regions (Solomon, 1999; Wang and Michelangeli, 2006; Harris et al., 2010; Wegner et al., 2012). Furthermore, the formation of these PSCs, and particularly of the nitric acid trihydrates (NAT), leads to a denitrification of the stratosphere (condensation of HNO_3 and further sedimentation towards the lower stratosphere), which prevents $ClONO_2$ to reform (Gobbi et al., 1991; Solomon, 1999; Ronsmans et al., 2016) and enhances further the depletion of ozone.

10   HNO_3 was measured by a variety of instruments in the last decades, amongst which the Microwave Limb Sounder (MLS, on the UARS, then the AURA satellite) provided the most complete data set. Its measurements started in 1991 and allowed extensive analyses on the seasonal and interannual variability, as well as on the vertical distribution of HNO_3 (Santee et al., 1999, 2004), with however a coarse horizontal resolution. Other instruments have also measured HNO_3 in the atmosphere, such as MIPAS (ENVISAT, Piccolo and Dudhia (2007)), ACE-FTS (SCISAT, Wang et al. (2007)) and SMR (ODIN, Urban et al.

15   (2009)), but few of these data have been used for geophysical analyses in terms of chemical and physical processes influencing HNO_3, mostly because of the limited horizontal sampling of these instruments.

On the other hand, O_3 has been extensively analysed, and numerous studies have been conducted to provide a better understanding of the factors influencing the stratospheric O_3 depletion processes and to assess the efficiency of the international treaties that were put in place to reduce its extent (Lary, 1997; Solomon, 1999; Morgenstern et al., 2008; Mäder et al., 2010;

20   Knibbe et al., 2014; Wespes et al., 2016). Most recent studies have used multivariate regression analyses in order to identify and quantify the main contributors to the O_3 spatial and seasonal variations. The variables included in such regression models depend on the atmospheric layer investigated (troposphere or stratosphere) and most often include the solar cycle, the quasi-biennial oscillation (QBO), the aerosol loading and the equivalent effective stratospheric chlorine (EESC) (Wohltmann et al., 2007; Sioris et al., 2014; de Laat et al., 2015). They often also include climate-related proxies for specific dynamical

25   patterns such as El Niño southern oscillation (ENSO), the North Atlantic Oscillation (NAO) or the Antarctic Oscillation (AAO) (Frossard et al., 2013; Rieder et al., 2013). Most often, the multivariate regression analyses use an iterative selection procedure to isolate the relevant variables for the concerned species (Mäder et al., 2007).

Despite the fact that it is one of the main species influencing stratospheric O_3, HNO_3 has much less been studied in terms of explanatory variables, in part because of the lack of global, consistent and sustained measurements. Identifying the factors

30   driving its spatial and temporal variability could help to characterize its behaviour in the stratospheric chemistry, and hence its interactions with O_3.

The Infrared Atmospheric Sounding Interferometer (IASI) onboard the Metop satellites has been and still is providing global measurements of the HNO_3 total column, which are used here to investigate the HNO_3 spatial and temporal variability. The data set used (Section 2) consists of time series of HNO_3 columns retrieved from IASI/Metop A measurements over the period

35   2008-2016, twice daily and with global coverage. The unprecedented spatial and temporal sampling of the high latitudes allows

Atmospheric
Chemistry
and Physics

Discussions

Open Access

for an in-depth monitoring of the atmospheric state in particular during the polar winter (Wespes et al., 2009; Ronsmans et al., 2016). We make use of equivalent latitudes in order to isolate polar air masses with specific polar vortex characteristics, and hence to better understand the role of HNO_3 in the polar chemistry, with regard to geophysical features such as the extent of the polar vortex and polar temperatures (Section 3). We next apply multivariate regressions to the IASI-derived HNO_3 time series

5　to statistically characterize their global distributions and seasonal variability for the first time, and this at different latitudes. The global coverage and the sampling of observations also allow retrieving global patterns of the main HNO_3 drivers (Section 4).

2　IASI HNO_3 data

The HNO_3 columns used here were retrieved from the measurements of the IASI instrument onboard the Metop A satellite. IASI measures the upwelling infrared radiation from the Earth's surface and the atmosphere in the 645-2760 cm^{-1} spectral

10　range at nadir and off nadir along a broad swath (2200 km). The level 1C data set used for the retrieval consists of bi-daily measurements (at 9:30 AM and PM, equator crossing time) at a 0.5 cm^{-1} apodized spectral resolution and with a low radiometric noise (0.2 K in the HNO_3 atmospheric window) (Clerbaux et al., 2009; Hilton et al., 2012). The ground field of view of the instrument consists of 4 elliptical pixels (2 by 2) yielding a horizontal footprint (single pixel) that varies from 113 km^2 (12 km diameter) at nadir to 400 km^2 at the end of the swath.

15　To retrieve HNO_3 atmospheric concentrations, we use the level 1C measurements available in near-real time at ULB and retrieved by the Fast Optimal Retrievals on Layers for IASI (FORLI) software, which uses the optimal estimation method (Rodgers, 2000). A complete description of the FORLI method can be found in Hurtmans et al. (2012) and a summary of the retrieval parameters specific to HNO_3 in Ronsmans et al. (2016). The retrieval initially yields HNO_3 vertical profiles on 41 levels (from 0 to 40 km altitude) but with limited vertical sensitivity. The characterization of the retrieved profiles

20　conducted by Ronsmans et al. (2016) showed indeed that the degrees of freedom for signal (DOFS) range from 0.9 to 1.2 at all latitudes. Because of this lack of vertical sensitivity, the HNO_3 total column is the most representative quantity for the IASI measurements and it is exploited here for the investigation of the HNO_3 time evolution. It is important to note, however, and as thoroughly discussed by Ronsmans et al. (2016), that the information on the HNO_3 profile comes mostly from the low-middle stratosphere (15-20 km) and that the profile is therefore mainly indicative of the stratospheric abundance. In

25　order to compute the total column, the retrieved vertical profiles are integrated over the whole altitude range. Our previous study showed that the resulting total columns yield a mean error of 10% and a low bias (10.5%) when compared to ground-based FTIR measurements (Ronsmans et al., 2016). The data set used spans from January 2008 to December 2016 with daily median HNO_3 columns averaged on a $2.5° \times 2.5°$ grid, for which both day and night measurements were used. Based on cloud information from the EUMETSAT operational processing, the cloud-contaminated scenes are filtered out, i.e. all scenes with a

30　higher fractional cloud cover than 25% are not taken into account. For the present study, the data are divided into several time series according to equivalent latitudes (sometimes here referred to as "eqlat") which allow to consider dynamically consistent regions of the atmosphere throughout the globe and to better preserve the sharp gradients across the edge of the polar vortex. The potential vorticity data are daily fields obtained from ECMWF ERA Interim reanalyses, taken at the potential temperature

of 530 K. Following the analysis of the potential vorticity contours, we consider 5 equivalent latitude bands in each hemisphere (30°-40°, 40°-55°, 55°-65°, 65°-70°, 70°-90°), plus the intertropical band (30°N - 30°S), with the corresponding potential vorticity contours, in units of $\times 10^{-6}$ K.m^2.kg^{-1}.s^{-1}, being at 2.5 (30°), 3 (40°), 5 (55°), 8 (65°) and 10 (70°) (Figure 1).

3 HNO$_3$ time series

5   The HNO$_3$ time series for the mid to high latitudes are displayed in Figure 2 for the years 2008-2016. Total columns are represented for both north (green) and south (blue curves) hemispheres, for equivalent latitudes bands 40-55°, 55-65°, 65-70° and 70-90°. Also highlighted by shaded areas are the periods during which the southern and northern polar temperatures, taken at 50 hPa (light blue and light green for the 70-90 eqlat band, S and N respectively, and purple for the 65-70 S eqlat band), were equal to or below the polar stratospheric clouds formation threshold (195 K, based on ECMWF temperatures). It

10   should be noted that this temperature corresponds to the formation threshold for NAT (type I), but that other forms of PSCs, particularly the type II PSCs (ice clouds) form at a lower temperature of 188 K (Santee et al., 1999; Wespes et al., 2009).

As a general rule, we find larger concentrations in the northern hemisphere, for the entire latitude range shown here (40-90 eqlat). The hemispheric difference in HNO$_3$ maximum concentrations can be partly attributed to the hemispheric asymmetry of the Brewer-Dobson circulation associated with the many topographical features in the northern hemisphere compared to the

15   southern hemisphere. As a result, the northern hemisphere has a more intense planetary wave activity, which strengthens the deep branch of the Brewer-Dobson circulation. This has also a direct effect on the latitudinal mixing processes, which usually extend into the Arctic polar region, but less into the Antarctic due to a stronger polar vortex (Mohanakumar, 2008; Butchart, 2014).

Further than the hemispheric asymmetry, we also find that the HNO$_3$ columns are generally larger at higher latitudes, with

20   total column maxima between 3.0×10^{16} and 3.7×10^{16} molec.cm^{-2} in the equivalent latitudes bands 70-90°, 65-70° and 55-65°, and lower at around 2.2×10^{16} molec.cm^{-2} in the 40-55° band, especially for the southern hemisphere. This latitudinal gradient of HNO$_3$ columns has been previously documented (Santee et al., 2004; Urban et al., 2009; Wespes et al., 2009; Ronsmans et al., 2016) and can be explained mainly by the larger amounts of NO$_y$ at high latitudes due to a larger age of air and by the NO$_y$ partitioning favoring HNO$_3$. Another interesting feature observable in Figure 2 is the different behaviour of

25   the three highest latitude regions with regard to the polar stratospheric clouds formation threshold in the southern hemisphere. The denitrification process that occurs with the condensation and sedimentation of PSCs (see Wespes et al. (2009); Manney et al. (2011) and Ronsmans et al. (2016) for further details) is obvious in the 70-90 S region (top panel, blue curve in Figure 2), with a systematic and strong decrease in HNO$_3$ total columns (from 3.3×10^{16} to 1.5×10^{16} molec.cm^{-2}) starting within 12 to 25 days after the stratospheric temperature reaches the threshold of 195 K (start of the blue shaded areas). The denitrification

30   thus usually starts around the beginning of June in the Antarctic and the concentrations reach their minimum value within one month. They stay low at 1.4×10^{16} molec.cm^{-2} until mid-November (with quite often a slight gradual increase to 1.7×10^{16} molec.cm^{-2} during the two following months), and start to increase again during January, i.e. between 2.5 and 3 months after the polar stratospheric temperatures are back above the NAT formation threshold. The same pattern can be observed in the

Atmospheric
Chemistry
and Physics
Discussions

65-70 S equivalent latitude region, with however, a delay of approximately 1 month for the start of the steepest decrease in HNO$_3$ columns, which appears to be more gradual than in the 70-90 S regions (3 months to reach the minimum values, starting in July). The minimum and plateau column values are thus reached by the end of September; they remain higher than at the highest latitudes, with values staying at around 1.7×10^{16} molec.cm^{-2}. The delayed and less severe denitrification in the 65-70

5   S band confirms that the denitrification process spreads from the center of the polar vortex, where the lowest temperatures are reached first. This spreading from the center also leads to slightly higher concentrations for the maxima in the 65-70 S eqlat band (mean of maxima of 3.26×10^{16}, versus 3.11×10^{16} molec.cm^{-2} in the 70-90 S eqlat band). The delayed denitrification in the outer parts of the vortex (i.e. in the 65-70 S eqlat band) can thus be attributed to the later appearance of PSCs (see Figure 2 purple shaded areas in second panel), and to the mixing of these air masses with the denitrified air masses from the

10   center of the vortex. These two processes lead to the total columns in both eqlat bands being in the same range of values by the end of December (1.7×10^{16} molec.cm^{-2}). If the decrease is slower at 65-70 eqlat, this is not the case for the recovery, with the build-up of concentrations that starts roughly at the same time as for the 70-90 S eqlat band, hence resulting in a shorter period of denitrified atmosphere in the 65-70 S band. These results agree well with previous studies by McDonald et al. (2000) and Santee et al. (2004) for earlier years. As for the 55-65 S eqlat band, which comprises the vortex rim itself, or

15   "collar" (Toon et al., 1989), it is evident from Figure 2, third panel, that it is not affected by denitrification, in agreement with previous observations (Santee et al. (1999); Wespes et al. (2009); Ronsmans et al. (2016)). In fact, we show that the columns in that band keep increasing during the low-temperature periods to reach maximum values of about 3.4×10^{16} molec.cm^{-2} in June-July; this is due to a change in the NO$_y$ partitioning towards HNO$_3$, itself due to less sunlight compared to lower latitudes. The slow decrease starting in August and leading to minimum values in January is related to the combined effect of increased

20   photodissociation and mixing with the denitrified polar air masses which are no more confined to the polar regions. Finally, as previously mentioned, the 40-55 S eqlat band records lower column values throughout the year (generally below 2×10^{16} molec.cm^{-2}) and a much less pronounced seasonal cycle.

The northern hemisphere high latitudes usually do not experience denitrification, mostly because the temperatures rarely reach the PSC formation threshold (see Figure 2, light green vertical areas). A few years stand out, however, with exceptionally

25   low stratospheric temperatures. This is especially the case of the 2011 (Manney et al., 2011), 2016 and, to some extent, 2014 winters. During these three winters, temperatures reached below the 195 K threshold and stayed low during a longer period than usual. Lower concentrations of HNO$_3$ have been recorded in consequence, especially in the northernmost equivalent latitude band (see Figure 2). The winter 2016 recorded in particular exceptionally low temperatures and led to large denitrification and significant ozone depletion (Manney and Lawrence, 2016; Matthias et al., 2016). The denitrification that occurred in the

30   northern polar regions affected a smaller area than what generally happens in the southern hemisphere; in particular the columns in the 65-70 N eqlat band do not show a significant decrease.

Figure 3, which consists in the time series of the zonally averaged distribution of the HNO$_3$ retrieved total columns, illustrates all these features particularly well: it highlights the low and constant columns between -40 and 40 degrees of latitude, the marked annual cycle at mid to high latitudes, the systematic and the occasional (2011, 2014, 2016) denitrification in the high

35   latitudes of the Southern and Northern hemispheres respectively, which are highlighted by the iso-contours of polar vorticity

at -10×10^{-6} K.m^2.kg^{-1}.s^{-1}.

In order to give further insights into the interannual variability in polar regions, Figure 4 shows the seasonal cycle for each individual year from 2008 to 2016 for eqlat 70-90 in the northern (top) and the southern (bottom) hemispheres. It should be noted that there was an abnormally small amount of IASI L2 data distributed by Eumetsat between the 14th of September and

5   the 2nd of December 2010 (Van Damme et al., 2017), and that these data have been removed from the Figure (see interrupted green curve). July and August of 2010 also stand out in the Antarctic, with high and variable columns recorded by IASI. Although we do not, at this stage, have a clear understanding of this, we hypothesize that this is a consequence of a mid-winter minor sudden stratospheric warming event that induced a downward motion of air masses and modified the chemical composition of the atmosphere between 10 and 50 hPa (de Laat and van Weele, 2011).

10   Apart from these peculiarities for the year 2010, all years seem to coincide quite well in terms of seasonality in the southern hemisphere (bottom panel). The timing of the denitrification is in particular consistent from one year to another. The northern hemisphere high latitudes (top panel) show more interannual variability especially because of the unusual dentrification periods observed in 2011 (purple), 2014 (blue) and 2016 (black) in January (concentrations as low as 2.2×10^{16} molec.cm^{-2} in 2016); during the summer, the columns are more stable around 2.1×10^{16} to 2.8×10^{16} molec.cm^{-2}.

15   ## 4   Fitting the observations with a regression model

4.1   Multi-variable linear regression

In order to identify the processes responsible for the HNO$_3$ variability observed in the IASI measurements, we use a multivariate linear regression model featuring various dynamical and chemical processes known to affect HNO$_3$ distributions. We follow strictly the methodology set-up by Wespes et al. (2016) for similarly investigating the O$_3$ variability. In particular, as in Wespes

20   et al. (2016), we use daily median HNO$_3$ total columns. These are fitted with the following model:

$$\text{HNO}_3(t) = cst + y_1.trend + [a_1.cos(\omega t) + b_1.sin(\omega t)] + \sum_{i=2}^{m} [y_i.Y_{\text{Norm,i}}(t)] + \epsilon(t) \tag{1}$$

where t is the day in the time series, the y terms are the regression coefficients for each variable, $\omega = 2\pi/365.25$, and $Y_{\text{Norm,i}}(t)$ refer to the chosen explanatory variables Y, which are normalized over the period of IASI observations (2008-2016) following:

25   $$Y_{\text{Norm,i}}(t) = 2(Y(t) - Y_{\text{median}})/(Y_{\text{max}} - Y_{\text{min}}) \tag{2}$$

with Y_{max} and Y_{min} the maximum and minimum values of the variable time series (before subtraction of the median, Y_{median}). The terms a_1 and b_1 in Eq.(1) are the coefficients accounting for the annual variability in the atmosphere. They account mainly for the seasonality of the solar insolation and of the meridional Brewer-Dobson circulation, which is a slow stratospheric circulation redistributing the tropical air masses to extra-tropical regions (Mohanakumar, 2008; Kyrölä et al., 2010).

Atmospheric
Chemistry
and Physics
Discussions

The regression coefficients are estimated by the least squares method. The standard error (σ_e) of each proxy is calculated based on the regression coefficients and is corrected in order to take the autocorrelation uncertainty into account (Knibbe et al., 2014; Wespes et al., 2016):

$$\sigma_e{}^2 = (\mathbf{Y}^\mathrm{T}\mathbf{Y})^{-1} \cdot \frac{\sum[\mathrm{HNO_3} - \mathbf{Y}y]^2}{n - m} \cdot \frac{1 + \varphi}{1 - \varphi} \tag{3}$$

5   where $\mathbf{Y}$ is the matrix of explanatory variables of size $n \times m$, n is the number of daily measurements and m the number of fitted parameters. $\mathrm{HNO_3}$ is the nitric acid column, y the vector of regression coefficients and φ is lag-1 autocorrelation of the residuals.

4.2   Iterative selection of explanatory variables

The choice of variables included in the model is made using an iterative elimination procedure; all variables are tested based
10   on their importance for the regression (Mäder et al., 2010). At each iteration, the variable with the largest p-value (and outside the confidence interval of 95%) is removed, until there remain only the variables relevant for the regression, i.e. the ones with a p-value smaller than 0.05. This selection algorithm is applied on each band of equivalent latitude (or grid cell, for the global distributions shown further) and thus yields a different combination of variables, depending on the equivalent latitude region considered.

4.3   Variables used for the regression

15

Given the strong relationship between the O_3 and the HNO_3 chemistry and variability (Solomon, 1999; Neuman et al., 2001; Santee et al., 2005; Popp et al., 2009) and the novelty in applying such a regression study in an HNO_3 dataset, we consider here the major and well known drivers of the total O_3 variability, namely: a linear trend, harmonic terms for the annual variability and geophysical proxies for the solar cycle, for the QBO and for the Arctic (AO) and Antarctic Oscillations (AAO) for the
20   northern and southern hemispheres, respectively. Considering the short length of the time series, however, the linear trend did not yield any significant result and, recalling that the aim of the paper is not to derive long term trends, this aspect will not be discussed further. In addition, a proxy for the volume of polar stratospheric clouds is included to account for the effect of the strong denitrification process during the polar night (cf. Section 3). All the proxies are shown in Figure 5 and described with more details hereafter. The source for each proxy is also provided in Table 1.

4.3.1   Solar flux (SF)

25

As a proxy for the solar activity, we use the 10.7 cm solar flux ($F_{10.7}$). It is a radio flux that varies daily, and correlates to the number of sunspots on the solar disk. The data set used here is the adjusted flux that takes the changing earth-sun distance into account. The solar cycle influences directly the partitioning between NO_y (produced by the $N_2O + O^1D$ reaction) and HNO_3 through the quantity of sunlight available, and has been known to affect the dynamics and to influence the O_3 response in the
30   lower stratosphere (Hood, 1997; Kodera and Kuroda, 2002; Hood and Soukharev, 2003; Austin et al., 2007).

4.3.2 Quasi-Biennial Oscillation (QBO)

The QBO is one of the main process regulating the dynamics of the tropical atmosphere (Baldwin et al., 2001; Sioris et al., 2014). It is driven by vertically propagating gravity waves, which lead to an oscillation between stratospheric winds blowing from east (easterlies) and from west (westerlies), with a period of about 28-29 months (Hauchecorne et al., 2010; Schirber, 2015). Its effect on the distribution of chemical species is significant, especially in equatorial regions where both a direct effect due to the changing winds and an indirect effect via its influence on the Brewer-Dobson circulation, affect, for example, the distribution of ozone (Lee and Smith, 2003; Mohanakumar, 2008; Frossard et al., 2013; Knibbe et al., 2014). Two monthly time series of QBO at two different pressure levels (30 hPa and 10 hPa) from ground-based measurements in Singapore have been considered for the present study, in order to take into account the differences in phase and shape of the QBO signal in the upper and lower stratosphere.

4.3.3 Multivariate ENSO Index (MEI)

The Multivariate ENSO Index is a metric that quantifies the strength of the El Niño-Southern Oscillation; it is computed based on the measurement of six variables over the tropical Pacific: sea-level pressure, zonal and meridonal winds, sea surface temperature, surface air temperature and cloudiness fraction. The ENSO phenomenon, even though it is a tropospheric process (mainly sea surface temperature contrasts), also affects stratospheric circulation. Previous studies have shown the impact of El Niño/La Niña oscillation on the stratospheric transport processes and the generation of Rossby waves, in turn modulating the strength of the polar vortex (Trenberth et al., 1998; Newman et al., 2001; Garfinkel et al., 2015) and affecting O_3 in the stratosphere (Randel et al., 2009; Lee et al., 2010; Randel and Thompson, 2011).

4.3.4 Arctic Oscillation and Antarctic Oscillation

The Arctic (AO) and Antarctic Oscillations (AAO) are included in the regression in order to represent the atmospheric variability observed in the northern and southern hemispheres, respectively. They are constructed from the daily geopotential height anomalies in the 20-90° region, at 1000 mb (for the northern hemisphere) and 700 mb (for the southern hemisphere). Each index is considered only in the hemisphere it is related to, while both indices are included for equatorial latitudes. The impact of these oscillations on O_3 distributions has been demonstrated in several studies (Rieder et al., 2013; Wespes et al., 2016). We may expect similar influence on the HNO_3 distributions, particularly because, even though they are tropospheric features, their phase and intensity affect the atmospheric circulation, and in particular the Brewer-Dobson Circulation, up to the stratosphere (Miller et al., 2006; Chehade et al., 2014).

4.3.5 Volume of Polar Stratospheric Clouds (VPSC)

The very low temperatures recorded during the winter in the polar stratosphere inside the vortex lead (from 195 K or T_{NAT} for the formation of nitric acid trihydrate particles) to the formation of polar stratospheric clouds (PSCs), which are composed either of nitric acid di- or trihydrates (NAD or NAT), supercooled ternary $HNO_3/H_2SO_4/H_2O$ solutions (STS) or water ice

(H$_2$O) (Wang and Michelangeli, 2006; Drdla and Müller, 2010). Here, we consider for the PSCs only the nitric acid trihydrate (NAT) particles (HNO$_3$.(H$_2$O)$_3$), which are ubiquitous (and often mixed with STS) (Voigt et al., 2000; Pitts et al., 2009; Lambert et al., 2016). The other forms of PSCs are expected to influence the variability in gaz-phase HNO$_3$ to a much lesser extent (von König et al., 2002).

5   The proxy we use here for the NAT is the volume of air below T_{NAT} (195 K), which depends on nitric acid concentrations, water vapor and pressure (Hanson and Mauersberger, 1988; Wohltmann et al., 2007). The temperatures needed to compute that quantity are based on ERA-Interim reanalyses and the HNO$_3$ and H$_2$O profiles are taken north and south of 70° from an MLS climatology. The proxy is calculated with a supersaturation of HNO$_3$ over NAT of 10, roughly corresponding to 3K supercooling (Hoyle et al., 2013; Lambert et al., 2016; Wohltmann et al., 2017). It should be noted that this proxy was not

10   included in the regression outside of the polar regions. Inside the polar regions (eqlat bands 70-90 north and south), it was included and subject to the selection algorithm.

Finally, it is worth to note that, for the sake of completeness, proxies accounting for the potential vorticity (PV) and for the Eliassen-Palm flux (EPflux) were also tested in order to take into account more precise patterns of the stratospheric dynamic and the Brewer-Dobson circulation. Also, various levels for the QBO were tested. However, none of these proxies lead to

15   a significant improvement of the residuals or the correlation coefficients, and their signal is therefore embedded here in the harmonic terms. For these reasons, they will not be discussed further.

4.4 Results

The results are presented in two ways: first, latitudinally averaged time series (eqlat bands) are used to analyze the performances of the fit in terms of correlation coefficients and residuals, with a focus on polar regions. The performance of the model is then

20   analysed in terms of global distributions (with the regression applied to every $2.5° \times 2.5°$ grid cell) and the spatial distribution of the fitted proxies is detailed.

4.4.1 HNO$_3$ fits for equivalent latitudes bands

For each eqlat band, the variables retained by the selection procedure (see Section 3.2) are listed in Table 2. Most variables are retained everywhere, except for the solar flux which is rejected in the polar latitudes (70-90 N and S). The QBO30 is also

25   excluded in the southern polar regions (65-90 S) and the MEI in the northern polar regions (65-90 N). Finally, the AO and AAO are excluded in the 65-70 N and in the 70-90 S, respectively.

The results from the multivariate regression are presented in Figure 6 for each band of equivalent latitude. The model reproduces well the measurements, with correlation coefficients between 0.81 (in the 30-40 N eqlat band) and 0.94 (in the 70-90 S eqlat bands). Most features (seasonal and interannual variabilities) are reproduced by the regression model. The residuals

30   range between 1.74×10^{10} and 9.44×10^{15} molec.cm^{-2}, with better results for the 30N-30S equivalent latitude band (RMSE of 2.39×10^{14} molec.cm^{-2}) and worse fits for the 65-70 S band (RMSE of 2.41×10^{15} molec.cm^{-2}). Following the comparison between the fits and the observational data, some features can be highlighted:

Atmospheric
Chemistry
and Physics
Discussions

- The high daily variability recorded in the data during the winter for both polar regions is not captured very well by the regression fit. Indeed, we find that the residuals are largest in this period, especially in the southern hemisphere during the denitrification period of each year (from June until September approximately), mostly because of the high variability of the vortex itself. There, we find an average standard deviation of 1.44×10^{16} molec.cm^{-2} (average of the standard deviation during the denitrification periods over the 8 years of observation), as opposed to a mean standard deviation of 8.30×10^{15} molec.cm^{-2} for the periods between the denitrifications. In the northern hemisphere, the day-to-day variability is largest during winter as well, when the vortex builds up, and this causes larger residuals for the corresponding months (see December through March of each year, top left panel of Figure 6, with an average standard deviation of 7.97×10^{15} molec.cm^{-2} to be compared to 7.26×10^{15} molec.cm^{-2} for the other months). It is important to stress that these larger residuals are obtained in the polar regions despite the fact that a VPSC proxy was used. In Figure 7 we show, however, that the regression model would perform worse in polar regions if that proxy is neglected, as also discussed here below.

- Even though the high variability during the denitrification periods is not reproduced exactly, the amplitude of the denitrification occurring in the Southern polar region is captured accurately by the regression model. Figure 7 shows a zoom of Figure 6 to better highlight the model performance during the denitrification periods; the regression was tested without (top panels) and with (middle panels) the VPSC proxy, for the 70-90 N (left panels) and the 70-90 S (right panels) eqlat bands. The steep slope observed at the start of the low temperatures is captured by the model when the proxy for the VPSC is included (Figure 7) and the correlation coefficients are better for both hemispheres (from 0.83 to 0.86 in the 70-90 N and from 0.84 to 0.94 in the 70-90 S eqlat band). In the 65-70 S eqlat band however, as previously described in Section 3, the HNO_3 columns continue to increase after the formation of PSCs has started in the 70-90 S eqlat band. This translates into a delay, in the fit for the 65-70 S eqlat band, in the drop of HNO_3 concentrations, which happens earlier than in the IASI observations since the VPSC proxy is based on temperatures and composition north of 70°. It translates to a lower correlation coefficient (0.87) and higher RMSE (2.41×10^{15} molec.cm^{-2}). A proxy adapted to this eqlat band should be used in further studies in order to represent the dynamic in that particular region of the vortex.

- The high maxima seen in the IASI time series, mostly from mid-April through the end of May in the Southern hemisphere, and from mid-December through early February in the Northern hemisphere, are not that well reproduced by the regression model. In fact, the model fails to capture the highest columns during the winters of each hemisphere. In the same way, a few strong lows recorded by IASI, especially those in the Northern polar regions after an exceptional denitrification has occurred (mid-June to early October 2014 and 2016, for instance) are not captured by the model.

Figure 8 shows the regression coefficients of each variable in each equivalent latitude band (top panel). The two bottom panels show the signal of the fitted proxies, calculated by multiplying the proxy by its regression coefficient. Only the variables retained by the selection algorithm are shown and discussed. From the top panel of Figure 8, it can be seen that all proxies are significant, with errors smaller than the coefficients for all eqlat bands. It is clear that the annual variability is predominant at all latitudes. From the two bottom panels, we also see the large influence of the VPSC in the regression for the polar regions.

Atmospheric
Chemistry
and Physics
Discussions

Their signal is, as expected, larger in the southern hemisphere where it reaches -1.3×10^{16} molec.cm^{-2}, which is to be compared to maximum values around -0.4×10^{16} molec.cm^{-2} in the northern hemisphere. A noteworthy difference is found for the year 2016 where the VPSC signal reached -0.7×10^{16} molec.cm^{-2} during the exceptionally cold Arctic winter. While the PSCs have significantly affected the HNO$_3$ distributions in the winters 2011, 2014 and 2016 in the Arctic, their influence during other

5 years may contribute to the high variability recorded in the observations (see Section 4.4.1). Other proxies show relatively large signals and their global distribution will be discussed further in Section 4.4.3.

4.4.2 Global model assessment with regard to the HNO$_3$ variability

To assess the model ability to reproduce the measurements, the top panel of Figure 9 shows the percentage of the HNO$_3$ variability seen by IASI that is explained by the regression model. The fraction is calculated as the difference between the

10 standard deviation of the fit and of the observations [σ (HNO_3^{fit}(t))/ σ (HNO_3^{IASI}(t)) × 100] and is expressed as a percentage. We find that most of the observed variability can be explained by the model in the southern hemisphere (between 50 and 80 %). The southern mid-latitudes and the polar regions are in particular well modeled (70-80 %), except in Antarctica above the ice shelves. The northern hemisphere HNO$_3$ variability is reasonably well explained by the model, particularly above 40° of latitude, with percentages ranging between 50 and 80 %, although some continental areas (Northern part of inner Eurasia)

15 stand out with percentages below 40 %. The region with the largest unexplained fraction of variability is the intertropical band extending as far as 40° north. There, the fraction of HNO$_3$ variability explained by the model reaches values as low as 20 %. These regions of low explained variability coincide quite well with the regions where a high lightning activity is found, which produces large amount of NO$_x$ in the troposphere (Labrador et al., 2004; Sauvage et al., 2007; Cooper et al., 2014). While the IASI instrument is usually not sensitive to tropospheric HNO$_3$, it was found that large amounts of tropospheric HNO$_3$ between

20 the tropics could be detected, mainly because of the lower contribution of the stratosphere in that region, and because the NO$_x$ emitted by lightning are released in the high troposphere, where IASI has still reasonable sensitivity. This could thus explain why the model is missing some of the variability recorded in the observational data. It should be noted that a small area of high explained variability is observed in Africa, just south of the equator. The variability in this region is unexpectedly high in the IASI time series (Figure 10) and we suggest that it could be influenced by biomass burning emissions of NO$_2$, and subsequent

25 oxydation to HNO$_3$ with a delay of about 2 months (Figure 10) (Scholes et al., 1996; Barbosa et al., 1999; Schreier et al., 2014). Indeed, the large vegetation fires of Africa every year around July emit the largest amounts of NO$_x$ (compared to large fires of South America, Australia and southeast Asia). If this hypothesis turns out to be true, it means that the annual term, which carries this variability in the regression model, is overrepresented in the fitted model. This larger contribution of the annual variability thus yields a better agreement between the observations and the model in the tropical band, however missing

30 some of the interannual variability due to these fires.

The bottom panel of Figure 9 depicts the global distribution of the root mean square error (RMSE) of the regression expressed as a percentage. The errors are small everywhere (between 10 and 20 %) except in the southern hemisphere above Antarctica, and particularly above the ice shelves (mainly the Ross and Ronne ice shelves). We also find higher values above the large desertic areas (the Sahara, the Arabian, the Turkestan and the Australian deserts) as well as off the west coasts of south Africa

Atmospheric
Chemistry
and Physics
Discussions

and South America where persistent low clouds occur. These regions of low clouds or characterized by sharp or seasonally varying emissivity features are known to cause problems for the retrieval of HNO_3 using the IASI spectra (Hurtmans et al., 2012; Ronsmans et al., 2016).

4.4.3 Global patterns of fitted parameters

5   Figure 11 shows the global distributions of the regression coefficients obtained after the multivariate regression, expressed in molec.cm^{-2}. All the variables are shown, with the areas where the proxy was not retained left blank. The contribution of each proxy to the HNO_3 variability was also calculated for each grid cell as $[\sigma(X_i)/\sigma(HNO_3^{IASI}) \times 100]$ with X_i referring to each of the i explanatory variables X, and expressed in %.

The annual cycle

10   The annual cycle, represented by the terms a_1 and b_1, shows large regression coefficients (Figure 11) and holds the largest part of the variability globally (up to 70% in the northern and southern mid to high latitudes), as was previously evidenced in Figure 8 (top panel). While the Brewer-Dobson circulation, which is embedded in these harmonic terms, influences to some extent the HNO_3 variability (through its influence on the conversion of N_2O to NO_y in the tropics and through the transport of NO_y-rich air masses towards the polar regions and subsequent transformation into HNO_3), the influence of the seasonality of the solar insolation is also likely to largely influence the annual seasonality, especially in the mid- to high latitudes. The

15   increasing columns recorded during the winter in both polar regions can be explained by the combination of three processes: first, at low temperatures, HNO_3 is formed by heterogeneous reactions between N_2O_5 and $H_2O_{aerosol}$ and between $ClONO_2$ and $H_2O_{aerosol}$ or $HCl_{aerosol}$, which add to the main source gas-phase reaction $OH+NO_2+M{\rightarrow}HNO_3$. Second, while the source reactions of HNO_3 are still active, the loss reactions (HNO_3 photolysis and its reaction with OH) are significantly slowed

20   down during the winter (Austin et al., 1986; McDonald et al., 2000; Santee et al., 2004). And third, with the decrease of the temperatures in the polar stratosphere, the winds inside the polar vortex gain intensity and induce a strong diabatic downward motion of air with little latitudinal mixing across the vortex boundary. This descending air from the upper stratosphere enriches the lower stratosphere in HNO_3 (Schoeberl and Hartmann, 1991; Manney et al., 1994; Santee et al., 1999).

The solar cycle, MEI, AO/AAO and QBO

25   The solar flux (SF), ENSO index (MEI) and Arctic and Antarctic Oscillation (AO and AAO, respectively, Figure 11) all have a similar influence in terms of magnitude (between -2.5×10^{15} and 2.5×10^{15} molec.cm^{-2}), although with different spatial patterns. The influence of the solar flux is positive in the northern polar latitudes and at the edge of eastern Antarctica, as well as above the Indian Ocean and Australia. It is close to zero or negative elsewhere.

The MEI shows a negative signal above the northern polar regions and in the eastern parts of the Pacific and Atlantic (especially

30   south of Africa) Oceans. A weak positive signal is observed above Australia and above the southern polar regions. Overall, the MEI influence is quite small, which is not surprising considering that it affects mostly the tropospheric circulation, where IASI

Atmospheric
Chemistry
and Physics
Discussions

is less sensitive. Its signature is nonetheless visible and significant in the eastern Pacific, where it contributes to up to 30% of the HNO_3 variability, and in the mid-latitudes of the northern hemisphere, similarly to what was reported for O_3 (Rieder et al., 2013).

The arctic oscillation (AO) signal is stronger, especially above the Atlantic Ocean, with a positive signal above eastern Canada
5   and Groenland and between the north of eastern Africa and Florida. Except for those two regions, the MEI contributes at mid to high latitudes of the northern hemisphere with a negative signal, which contributes for $10 - 20\%$ to the HNO_3 variability. The corresponding proxy for the southern hemisphere (AAO) is also significant, with a strong positive signal above the vortex rim and a negative signal above Antarctica. These results are in agreement with previous studies that showed that, for O_3, both the arctic and antarctic oscillations (also called "annular modes") are the leading modes of variation in the extratropical
10   atmosphere. They largely influence the circulation up to the lower stratosphere and represent, particularly in the southern hemisphere, the fluctuations in the strength of the polar vortex (Thompson and Wallace, 2000; Jones and Widmann, 2004; van den Broeke and van Lipzig, 2004; Wespes et al., 2009). This further shows the strong correlation in the behaviour of O_3 and HNO_3.

The QBO has a generally small influence on the distributions with, however, some contribution (up to 30%) in the equatorial
15   band as expected (Baldwin et al., 2001; Solomon et al., 2014). As previously mentioned, several tests have been performed (not shown here) with the QBO taken at other pressure levels in the atmosphere (namely 20 and 50 hPa), and similar results have been obtained.

VPSC

The annual cycle, which is the dominant factor for HNO_3 variability at all latitudes, leading to the build-up of concentrations
20   during the winter, is interrupted in the southern polar regions, particularly in the 70-90 S eqlat band (see also Figure 8), by the condensation and further sedimenation of PSCs. The VPSC proxy, reflecting the volume of air below T_{NAT}, has a strong anti-correlated effect on HNO_3 columns, which decrease (negative values) with increasing VPSC (Wang and Michelangeli, 2006; Lowe and MacKenzie, 2008; Kirner et al., 2015). The signal of the VPSC proxy is thus, as expected, negative everywhere (in the polar regions considered), with values around -6×10^{15} molec.cm^{-2}. When looking at their contribution, we find that the
25   VPSC account for a larger part of the variability ($40 - 60\%$) in the southern hemisphere, where the influence of denitrification is indeed expected to be more important, compared to the northern hemisphere (maxima of 40%), as discussed in Section 3 with the analysis of Figure 2. The small areas with a positive signal appear to be non significant (see grey crosses).

5   Conclusions

Time series of HNO_3 total columns retrieved from IASI/Metop between 2008 and 2016 have been presented and analyzed in
30   terms of seasonal cycle and global variability. The analysis was conducted in terms of equivalent latitudes (here calculated on the basis of potential vorticity) and focused mainly on high latitude regions. We have shown that the IASI instrument captures the broad patterns of the seasonal cycles at all latitudes but also year-to-year specific behaviours. The systematic denitrification

Atmospheric
Chemistry
and Physics
Discussions

process occurring every winter-spring in the southern hemisphere shows up unambiguously in the time evolutions and the use of equivalent latitudes has enabled to isolate the regions affected based on the dominating stratospheric dynamical regimes. Three distinct zones within the polar regions were in particular separated; 1) the inner polar region (70-90 S), where the denitrification starts the earliest and where the HNO_3 columns reach their lowest values for the longest period; 2) the outer part

5　of the polar vortex (65-70 S), where the HNO_3 columns drop occurs 1 month later and the minimum concentrations do not reach such low levels; 3) the polar vortex edges (55-65 S), where the columns follow a more normal annual cycle, with maxima around July, forming a collar of high columns around the denitrified vortex. The IASI-derived HNO_3 distributions also reveal the unusual denitrification periods in the northern hemisphere, during the exceptionally cold winters of 2011, 2014 and 2016. The HNO_3 time series have been successfully fitted with multivariate regressions in order to identify the various factors re-

10　sponsible for the variability in the observations. To the best of our knowledge, this is the first time that such regression models are applied to the HNO_3 time evolution. A specific set of explanatory variables was retained for each equivalent latitude band following an iterative procedure, according to the influence of each of these variables in the regression. The regression model allowed good representation of the IASI observations in most cases (correlation coefficients between 0.81 and 0.94). However, the variability recorded between the tropics could not be reproduced that well, with only about 20 to 40 % correctly accounted

15　for. The regression for other parts of the globe yielded better results, especially in the southern polar regions, where a high percentage (60-80 %) of the observed variability is reproduced by the regression. Generally, it was found that the annual cycle is the factor responsible for the largest part of the variability, showing a hemispheric pattern. The Brewer-Dobson circulation, and also the solar insolation seasonality, which are embedded in the harmonic terms, seem to be the main drivers of variability, with the Brewer-Dobson circulation carrying NO_y towards the poles and both processes bringing the HNO_3 concentrations to

20　their maxima during the local winter when production is enhanced and destruction inhibited (Mohanakumar, 2008; Butchart, 2014; Konopka et al., 2015). We show interestingly that the polar stratospheric clouds contribute as the second most important driver of the variability of HNO_3 in the southern polar latitudes (65-90 S). The influence of PSCs is as expected less marked in the northern hemisphere, but still allow improving significantly the model-to-observation agreement especially during the colder northern winters (R from 0.83 to 0.86). While we feel that the VPSC proxy used here for the PSCs (including only the

25　NAT) is generally good, it is not excluded that adding other forms of PSCs would further improve the model. In any case, the present work shows the potential of using the IASI measurements to study in depth the polar denitrification processes.

Going towards to the mid- and tropical latitudes, the annual cycle is still prominent, but the relative influence of the QBO increases. Most of the weak seasonality revealed by IASI in the tropical regions is explained by the annual cycle (as well as a potential contribution of African fires and of lightning for additional NO_x sources), the QBO and the MEI.

30　More generally, this study shows that the IASI data allow a good analysis and understanding of the HNO_3 variability in the atmosphere. The measurements are made with exceptional spatial and temporal sampling, which allows a detailed analysis of the polar regions throughout the entire year. The amount of data allows isolating statistically relevant features in the variability, such as the denitrification processes in the southern polar regions. The IASI HNO_3 time series will soon be extended with the launch of Metop C in September 2018, which should further improve the regression model. As shown here by the still

significant residuals at some periods and locations, other factors could also probably be included to acquire a full and coherent representation of the HNO$_3$ total columns variability.

Atmospheric
Chemistry
and Physics
Discussions

References

Austin, J., Garcia, R. R., Russell, J. M., Solomon, S., and Tuck, A. F.: On the Atmospheric Photochemistry of Nitric Acid, Journal of Geophysical Research, 91, 5477–5485, https://doi.org/10.1029/JD091iD05p05477, 1986.

Austin, J., Hood, L. L., and Soukharev, B. E.: Solar cycle variations of stratospheric ozone and temperature in simulations of a coupled
5   chemistry-climate model, Atmospheric Chemistry and Physics, 7, 1693–1706, https://doi.org/10.5194/acp-7-1693-2007, 2007.

Baldwin, M. P., Gray, L. J., Dunkerton, T. J., Hamilton, K., Haynes, P. H., Holton, J. R., Alexander, M. J., Hirota, I., Horinouchi, T., Jones, D. B. A., Marquardt, C., Sato, K., and Takahashi, M.: The quasi-biennial oscillation, Reviews of Geophysics, 39, 179–229, http://dx.doi.org/10.1029/1999RG000073, 2001.

Barbosa, P. M., Stroppiana, D., Grégoire, J., and Pereira, J. M. C.: An assessment of vegetation fire in Africa (1981-1991): Burned areas,
10   burned biomass, and atmospheric emissions, Global Biogeochemical Cycles, 13, 933–950, https://doi.org/10.1029/1999GB900042, 1999.

Butchart, N.: The Brewer-Dobson circulation, Rev. Geophys, 52, 157–184, https://doi.org/10.1002/2013RG000448, 2014.

Chehade, W., Weber, M., and Burrows, J. P.: Total ozone trends and variability during 1979–2012 from merged data sets of various satellites, Atmospheric Chemistry and Physics, 14, 7059–7074, https://doi.org/10.5194/acp-14-7059-2014, 2014.

Clerbaux, C., Boynard, A., Clarisse, L., George, M., Hadji-Lazaro, J., Herbin, H., Hurtmans, D., Pommier, M., Razavi, A., Turquety, S.,
15   Wespes, C., and Coheur, P.-F.: Monitoring of atmospheric composition using the thermal infrared IASI/MetOp sounder, Atmospheric Chemistry and Physics, 9, 6041–6054, https://doi.org/10.5194/acp-9-6041-2009, 2009.

Cooper, M., Martin, R. V., Wespes, C., Coheur, P.-F., Clerbaux, C., and Murray, L. T.: Tropospheric nitric acid columns from the IASI satellite instrument interpreted with a chemical transport model: Implications for parametrizations of nitric oxide production by lightning, Journal of Geophysical Research, 119, 68–79, https://doi.org/10.1002/2014JD021907, 2014.

20 de Laat, A. T. J. and van Weele, M.: The 2010 Antarctic ozone hole: Observed reduction in ozone destruction by minor sudden stratospheric warmings, Scientific Reports, 1, 38, https://doi.org/10.1038/srep00038, 2011.

de Laat, A. T. J., van der A, R. J., and van Weele, M.: Tracing the second stage of ozone recovery in the Antarctic ozone-hole with a "big data" approach to multivariate regressions, Atmospheric Chemistry and Physics, 15, 79–97, https://doi.org/10.5194/acp-15-79-2015, 2015.

Drdla, K. and Müller, R.: Temperature thresholds for polar stratospheric ozone loss, Atmospheric Chemistry and Physics Discussions, 10,
25   28 687–28 720, https://doi.org/10.5194/acpd-10-28687-2010, 2010.

Fischer, H., Waibel, A. E., Welling, M., Wienhold, F. G., Zenker, T., Crutzen, P. J., Arnold, F., Bürger, V., Schneider, J., Bregman, A., Lelieveld, J., and Siegmund, P. C.: Observations of high concentration of total reactive nitrogen (NOy) and nitric acid (HNO3) in the lower Arctic stratosphere during the Stratosphere-Troposphere Experiment by Aircraft Measurements (STREAM) II campaign in February 1995, Journal of Geophysical Research, 102, 23 559, https://doi.org/10.1029/97JD02012, 1997.

30 Frossard, L., Rieder, H. E., Ribatet, M., Staehelin, J., Maeder, J. A., Di Rocco, S., Davison, A. C., and Peter, T.: On the relationship between total ozone and atmospheric dynamics and chemistry at mid-latitudes – Part 1: Statistical models and spatial fingerprints of atmospheric dynamics and chemistry, Atmospheric Chemistry and Physics Discussions, 12, 13 161–13 199, https://doi.org/10.5194/acp-13-147-2013, 2013.

Garfinkel, C. I., Hurwitz, M. M., and Oman, L. D.: Effect of recent sea surface temperature trends on the Arctic stratospheric vortex, Journal
35   of Geophysical Research Atmospheres, 120, 5404–5416, https://doi.org/10.1002/2015JD023284, 2015.

Gobbi, G. P., Deshler, T., Adriani, A., and Hofmann, D. J.: Evidence for denitrification in the 1990 Antarctic spring stratosphere: I, Lidar and temperature measurements, Geophysical Research Letters, 18, 1995–1998, https://doi.org/10.1029/91GL02310, 1991.

Atmospheric
Chemistry
and Physics
Discussions

Hanson, D. and Mauersberger, K.: Laboratory studies of the nitric acid trihydrate: Implications for the south polar stratosphere, Geophysical Research Letters, 15, 855–858, https://doi.org/10.1029/GL015i008p00855, 1988.

Harris, N. R. P., Lehmann, R., Rex, M., and von der Gathen, P.: A closer look at Arctic ozone loss and polar stratospheric clouds, Atmospheric Chemistry and Physics, 10, 8499–8510, https://doi.org/10.5194/acp-10-8499-2010, 2010.

5 Hauchecorne, A., Bertaux, J. L., Dalaudier, F., Keckhut, P., Lemennais, P., Bekki, S., Marchand, M., Lebrun, J. C., Kyrölä, E., Tamminen, J., Sofieva, V., Fussen, D., Vanhellemont, F., Fanton Dandon, O., Barrot, G., Blanot, L., Fehr, T., and Saavedra De Miguel, L.: Response of tropical stratospheric O3, NO2 and NO3 to the equatorial Quasi-Biennial Oscillation and to temperature as seen from GOMOS/ENVISAT, Atmospheric Chemistry and Physics, 10, 8873–8879, https://doi.org/10.5194/acp-10-8873-2010, 2010.

Hilton, F., Armante, R., August, T., Barnet, C., Bouchard, A., Camy-Peyret, C., Capelle, V., Clarisse, L., Clerbaux, C., Coheur, P.-F., Collard,
10   A., Crevoisier, C., Dufour, G., Edwards, D., Faijan, F., Fourrié, N., Gambacorta, A., Goldberg, M., Guidard, V., Hurtmans, D., Illingworth, S., Jacquinet-Husson, N., Kerzenmacher, T., Klaes, D., Lavanant, L., Masiello, G., Matricardi, M., McNally, A., Newman, S., Pavelin, E., Payan, S., Péquignot, E., Peyridieu, S., Phulpin, T., Remedios, J., Schlüssel, P., Serio, C., Strow, L., Stubenrauch, C., Taylor, J., Tobin, D., Wolf, W., and Zhou, D.: Hyperspectral Earth Observation from IASI: Five Years of Accomplishments, Bulletin of the American Meteorological Society, 93, 347–370, https://doi.org/10.1175/BAMS-D-11-00027.1, 2012.

15 Hood, L. L.: The solar cycle variation of total ozone: Dynamical forcing in the lower stratosphere, J. Geophys. Res., 102, 1355–1370, https://doi.org/10.1029/2007JD009391, 1997.

Hood, L. L. and Soukharev, B. E.: Quasi-Decadal Variability of the Tropical Lower Stratosphere: The Role of Extratropical Wave Forcing, Journal of the Atmospheric Sciences, 60, 2389–2403, https://doi.org/10.1175/1520-0469(2003)060<2389:QVOTTL>2.0.CO;2, 2003.

Hoyle, C. R., Engel, I., Luo, B. P., Pitts, M. C., Poole, L. R., Grooß, J. U., and Peter, T.: Heterogeneous formation of polar stratospheric clouds-
20   Part 1: Nucleation of nitric acid trihydrate (NAT), Atmospheric Chemistry and Physics, 13, 9577–9595, https://doi.org/10.5194/acp-13-9577-2013, 2013.

Hurtmans, D., Coheur, P.-F., Wespes, C., Clarisse, L., Scharf, O., Clerbaux, C., Hadji-Lazaro, J., George, M., and Turquety, S.: FORLI radiative transfer and retrieval code for IASI, Journal of Quantitative Spectroscopy and Radiative Transfer, 113, 1391–1408, https://doi.org/10.1016/j.jqsrt.2012.02.036, 2012.

25 Jones, J. M. and Widmann, M.: Early peak in Antarctic oscillation index, Nature, 432, 290–291, https://doi.org/10.1038/432290b, 2004.

Kirner, O., Müller, R., Ruhnke, R., and Fischer, H.: Contribution of liquid, NAT and ice particles to chlorine activation and ozone depletion during Antarctic winter and spring, Atmospheric Chemistry and Physics, 15, 2019–2030, https://doi.org/10.5194/acp-15-2019-2015, 2015.

Knibbe, J. S., van der A, R. J., and de Laat, A. T. J.: Spatial regression analysis on 32 years of total column ozone data, Atmospheric Chemistry and Physics, 14, 8461–8482, https://doi.org/10.5194/acp-14-8461-2014, 2014.

30 Kodera, K. and Kuroda, Y.: Dynamical response to the solar cycle, Journal of Geophysical Research Atmospheres, 107, 1–12, https://doi.org/10.1029/2002JD002224, 2002.

Konopka, P., Ploeger, F., Tao, M., Birner, T., and Riese, M.: Hemispheric asymmetries and seasonality of mean age of air in the lower stratosphere: Deep versus shallow branch of the Brewer-Dobson circulation, Journal of Geophysical Research: Atmospheres, 120, https://doi.org/10.1002/2014JD022429.Received, 2015.

35 Kyrölä, E., Tamminen, J., Sofieva, V., Bertaux, J. L., Hauchecorne, A., Dalaudier, F., Fussen, D., Vanhellemont, F., Fanton D'Andon, O., Barrot, G., Guirlet, M., Fehr, T., and Saavedra De Miguel, L.: GOMOS O3, NO2, and NO3 observations in 2002-2008, Atmospheric Chemistry and Physics, 10, 7723–7738, https://doi.org/10.5194/acp-10-7723-2010, 2010.

Labrador, L. J., Von Kuhlmann, R., and Lawrence, M. G.: Strong sensitivity of the global mean OH concentration and the tropospheric oxidiz-ing efficiency to the source of NOx from lightning, Geophysical Research Letters, 31, L06 102, https://doi.org/10.1029/2003GL019229, 2004.

Lambert, A., Santee, M. L., and Livesey, N. J.: Interannual variations of early winter Antarctic polar stratospheric cloud formation and nitric acid observed by CALIOP and MLS, Atmospheric Chemistry and Physics, 16, 15 219–15 246, https://doi.org/10.5194/acp-16-15219-2016, 2016.

Lary, D. J.: Catalytic destruction of stratospheric ozone, Journal of Geophysical Research, 102, 21 515–21 526, https://doi.org/10.1029/97JD00912, 1997.

Lee, H. and Smith, A. K.: Simulation of the combined effects of solar cycle, quasi-biennial oscillation, and volcanic forcing on stratospheric ozone changes in recent decades, Journal of Geophysical Research, 108, 1–16, https://doi.org/10.1029/2001JD001503, 2003.

Lee, S., Shelow, D. M., Thompson, A. M., and Miller, S. K.: QBO and ENSO variability in temperature and ozone from SHADOZ, 1998-2005, Journal of Geophysical Research Atmospheres, 115, 1998–2005, https://doi.org/10.1029/2009JD013320, 2010.

Lowe, D. and MacKenzie, A. R.: Polar stratospheric cloud microphysics and chemistry, Journal of Atmospheric and Solar-Terrestrial Physics, 70, 13–40, https://doi.org/10.1016/j.jastp.2007.09.011, 2008.

Mäder, J. A., Staehelin, J., Brunner, D., Stahel, W. A., Wohltmann, I., and Peter, T.: Statistical modeling of total ozone: Selection of appro-priate explanatory variables, Journal of Geophysical Research, 112, https://doi.org/10.1029/2006JD007694, 2007.

Mäder, J. A., Staehelin, J., Peter, T., Brunner, D., Rieder, H. E., and Stahel, W. A.: Evidence for the effectiveness of the Montreal Protocol to protect the ozone layer, Atmospheric Chemistry and Physics, 10, 12 161–12 171, https://doi.org/10.5194/acp-10-12161-2010, 2010.

Manney, G. L. and Lawrence, Z. D.: The major stratospheric final warming in 2016: Dispersal of vortex air and termination of Arctic chemical ozone loss, Atmospheric Chemistry and Physics, 16, 15 371–15 396, https://doi.org/10.5194/acp-16-15371-2016, 2016.

Manney, G. L., Zurek, R., O'Neill, A., and Swinbank, R.: On the motion of air through the stratospheric polar vortex, Journal of the Atmospheric Sciences, 51, 2973–2994, https://doi.org/10.1175/1520-0469(1994)051<2973:OTMOAT>2.0.CO;2, 1994.

Manney, G. L., Santee, M. L., Rex, M., Livesey, N. J., Pitts, M. C., Veefkind, P., Nash, E. R., Wohltmann, I., Lehmann, R., Froidevaux, L., Poole, L. R., Schoeberl, M. R., Haffner, D. P., Davies, J., Dorokhov, V., Gernandt, H., Johnson, B., Kivi, R., Kyrö, E., Larsen, N., Levelt, P. F., Makshtas, A., McElroy, C. T., Nakajima, H., Parrondo, M. C., Tarasick, D. W., von der Gathen, P., Walker, K. A., and Zinoviev, N. S.: Unprecedented Arctic ozone loss in 2011, Nature, 478, 469–475, https://doi.org/10.1038/nature10556, 2011.

Matthias, V., Dörnbrack, A., and Stober, G.: The extraordinarily strong and cold polar vortex in the early northern winter 2015/2016, Geo-physical Research Letters, 43, 12,287–12,294, https://doi.org/10.1002/2016GL071676, 2016.

McDonald, M., de Zafra, R., and Muscari, G.: Millimeter wave spectroscopic measurements over the South Pole 5 . Morphol-ogy and evolution of HNO3 vertical distribution, 1993 versus 1995, Journal of Geophysical Research, 105, 17 739–17 750, https://doi.org/10.1029/2000JD900120, 2000.

Miller, A. J., Cai, A., Tiao, G., Wuebbles, D. J., Flynn, L. E., Yang, S. K., Weatherhead, E. C., Fioletov, V., Petropavlovskikh, I., Meng, X. L., Guillas, S., Nagatani, R. M., and Reinsel, G. C.: Examination of ozonesonde data for trends and trend changes incorporating solar and Arctic oscillation signals, Journal of Geophysical Research: Atmospheres, 111, 1–10, https://doi.org/10.1029/2005JD006684, 2006.

Mohanakumar, K.: Stratosphere Troposphere Interactions - An Introduction, https://doi.org/10.1007/978-1-4020-8217-7, 2008.

Morgenstern, O., Braesicke, P., Hurwitz, M. M., O'Connor, F. M., Bushell, A. C., Johnson, C. E., and Pyle, J. A.: The world avoided by the Montreal Protocol, Geophysical Research Letters, 35, 1–5, https://doi.org/10.1029/2008GL034590, 2008.

Neuman, J. A., Gao, R. S., Fahey, D. W., Holecek, J. C., Ridley, B. A., Walega, J. G., Grahek, F. E., Richard, E. C., McElroy, C. T., Thompson, T. L., Elkins, J. W., Moore, F. L., and Ray, E. A.: In situ measurements of HNO3 , NOy , NO , and O3 in the lower stratosphere and upper troposphere, Atmospheric Environment, 35, 5789–5797, https://doi.org/10.1016/S1352-2310(01)00354-5, 2001.

Newman, P. A., Nash, E. R., and Rosenfield, J. E.: What controls the temperature of the Arctic stratosphere during the spring?, Journal of
5   Geophysical Research, 106, 19 999–20 010, https://doi.org/10.1029/2000jd000061, 2001.

Piccolo, C. and Dudhia, A.: Precision validation of MIPAS-Envisat products, Atmospheric Chemistry and Physics, 7, 1915–1923, https://doi.org/10.5194/acp-7-1915-2007, 2007.

Pitts, M. C., Poole, L. R., and Thomason, L. W.: CALIPSO polar stratospheric cloud observations: second-generation detection algorithm and composition discrimination, Atmospheric Chemistry and Physics, 9, 7577–7589, https://doi.org/10.5194/acp-9-7577-2009, 2009.

10   Popp, P. J., Marcy, T. P., Gao, R. S., Watts, L. A., Fahey, D. W., Richard, E. C., Oltmans, S. J., Santee, M. L., Livesey, N. J., Froidevaux, L., Sen, B., Toon, G. C., Walker, K. A., Boone, C. D., and Bernath, P. F.: Stratospheric correlation between nitric acid and ozone, Journal of Geophysical Research, 114, D03 305, https://doi.org/10.1029/2008JD010875, 2009.

Randel, W. J. and Thompson, A. M.: Interannual variability and trends in tropical ozone derived from SAGE II satellite data and SHADOZ ozonesondes, Journal of Geophysical Research Atmospheres, 116, 1–9, https://doi.org/10.1029/2010JD015195, 2011.

15   Randel, W. J., Garcia, R. R., Calvo, N., and Marsh, D.: ENSO influence on zonal mean temperature and ozone in the tropical lower stratosphere, Geophysical Research Letters, 36, 1–5, https://doi.org/10.1029/2009GL039343, 2009.

Rieder, H. E., Frossard, L., Ribatet, M., Staehelin, J., Maeder, J. A., Di Rocco, S., Davison, A. C., Peter, T., Weihs, P., and Holawe, F.: On the relationship between total ozone and atmospheric dynamics and chemistry at mid-latitudes – Part 2: The effects of the El Niño/Southern Oscillation, volcanic eruptions and contributions of atmospheric dynamics and chemistry to long-term total ozone, Atmospheric Chemistry
20   and Physics, 12, 13 201–13 236, https://doi.org/https://doi.org/10.5194/acp-13-165-2013, 2013.

Rodgers, C. D.: Inverse Methods for Atmospheric Sounding - Theory and Practice, vol. 2 of *Series on Atmospheric Oceanic and Planetary Physics*, World Scientific Publishing Co. Pte. Ltd., https://doi.org/10.1142/9789812813718, 2000.

Ronsmans, G., Langerock, B., Wespes, C., Hannigan, J. W., Hase, F., Kerzenmacher, T., Mahieu, E., Schneider, M., Smale, D., Hurtmans, D., De Mazière, M., Clerbaux, C., and Coheur, P.-F.: First characterization and validation of FORLI-HNO3 vertical profiles retrieved from
25   IASI/Metop, Atmospheric Measurement Techniques, 9, 4783–4801, https://doi.org/10.5194/amt-9-4783-2016, 2016.

Santee, M. L., Manney, G. L., Froidevaux, L., Read, W. G., and Waters, J. W.: Six years of UARS Microwave Limb Sounder HNO3 observations : Seasonal, interhemispheric, and interannual variations in the lower stratosphere, Journal of Geophysical Research, 104, 8225–8246, https://doi.org/10.1029/1998JD100089, 1999.

Santee, M. L., Manney, G. L., Livesey, N. J., and Read, W. G.: Three-dimensional structure and evolution of stratospheric
30   HNO3 based on UARS microwave limb sounder measurements, Journal of Geophysical Research D: Atmospheres, 109, 1–19, https://doi.org/10.1029/2004JD004578, 2004.

Santee, M. L., Manney, G. L., Livesey, N. J., Froidevaux, L., MacKenzie, I. A., Pumphrey, H. C., Read, W. G., Schwartz, M. J., Waters, J. W., and Harwood, R. S.: Polar processing and development of the 2004 Antarctic ozone hole: First results from MLS on Aura, Geophysical Research Letters, 32, 1–4, https://doi.org/10.1029/2005GL022582, 2005.

35   Sauvage, B., Martin, R. V., van Donkelaar, A., and Ziemke, J. R.: Quantification of the factors controlling tropical tropospheric ozone and the South Atlantic maximum, Journal of Geophysical Research Atmospheres, 112, 1–14, https://doi.org/10.1029/2006JD008008, 2007.

Schirber, S.: Influence of ENSO on the QBO: Results from an ensemble of idealized simulations, Journal of Geophysical Research: Atmospheres, 120, 1109–1122, https://doi.org/10.1002/2014JD022460, 2015.

Schoeberl, M. R. and Hartmann, D. L.: The Dynamics of the Stratospheric Polar Vortex and Its Relation to Springtime Ozone Depletions, Science, 251, 46–52, https://doi.org/10.1126/science.251.4989.46, 1991.

Scholes, R., Ward, D., and Justice, C.: Emissions of trace gases and aerosol particles due to vegetation burning in southern hemisphere Africa, Journal of Geophysical Research, 101, 23 677–23 682, https://doi.org/10.1029/95JD02049, 1996.

5 Schreier, S. F., Richter, A., Kaiser, J. W., and Burrows, J. P.: The empirical relationship between satellite-derived tropospheric NO2 and fire radiative power and possible implications for fire emission rates of NOx, Atmospheric Chemistry and Physics, 14, 2447–2466, https://doi.org/10.5194/acp-14-2447-2014, 2014.

Sioris, C. E., McLinden, C. A., Fioletov, V. E., Adams, C., Zawodny, J. M., Bourassa, A. E., Roth, C. Z., and Degenstein, D. A.: Trend and variability in ozone in the tropical lower stratosphere over 2.5 solar cycles observed by SAGE II and OSIRIS, Atmospheric Chemistry and

10 Physics, 14, 3479–3496, https://doi.org/10.5194/acp-14-3479-2014, 2014.

Solomon, A., Richter, J. H., and Bacmeister, J. T.: An objective analysis of the QBO in ERA-Interim and the Community Atmosphere Model, version 5, Geophysical Research Letters, 41, 7791–7798, https://doi.org/10.1002/2014GL061801, 2014.

Solomon, S.: Stratospheric ozone depletion: A review of concepts and history, Reviews of Geophysics, 37, 275–316, https://doi.org/10.1029/1999RG900008, 1999.

15 Thompson, D. W. J. and Wallace, J. M.: Annular Modes in the Extratropical Circulation. Part I : Month-to-Month Variability, Journal of Climate, 13, 1000–1016, https://doi.org/http://dx.doi.org/10.1175/1520-0442(2000)013<1000:AMITEC>2.0.CO;2, 2000.

Toon, G. C., Farmer, C. B., Lowes, L. L., Schaper, P. W., Blavier, J., and Norton, R. H.: Infrared Aircraft Measurements of Stratospheric Composition Over Antarctica During September 1987, Journal of Geophysical Research, 94, 16 571–16 596, https://doi.org/10.1029/JD094iD14p16571, 1989.

20 Trenberth, K. E., Branstator, G. W., Karoly, D., Kumar, A., Lau, N.-C., and Ropelewski, C.: Progress during TOGA in understanding and modeling global teleconnections associated with tropical sea surface temperatures, Journal of Geophysical Research: Oceans, 103, 14 291–14 324, https://doi.org/10.1029/97JC01444, 1998.

Urban, J., Pommier, M., Murtagh, D. P., Santee, M. L., and Orsolini, Y. J.: Nitric acid in the stratosphere based on Odin observations from 2001 to 2009 – Part 1 : A global climatology, Atmospheric Chemistry and Physics, 9, 7031–7044, https://doi.org/10.5194/acp-9-7031-

25 2009, 2009.

Valks, P., Pinardi, G., Richter, A., Lambert, J. C., Hao, N., Loyola, D., Van Roozendael, M., and Emmadi, S.: Operational total and tropospheric NO2 column retrieval for GOME-2, Atmospheric Measurement Techniques, 4, 1491–1514, https://doi.org/10.5194/amt-4-1491-2011, 2011.

Van Damme, M., Whitburn, S., Clarisse, L., Clerbaux, C., Hurtmans, D., and Coheur, P.-F.: Version 2 of the IASI NH3 neural

30 network retrieval algorithm; near-real time and reanalysed datasets, Atmospheric Chemistry and Physics Discussions, pp. 1–14, https://doi.org/https://doi.org/10.5194/amt-2017-239, 2017.

van den Broeke, M. R. and van Lipzig, N. P. M.: Changes in Antarctic temperature, wind and precipitation in response to the Antarctic Oscillation, Annals of Glaciology, 39, 119–126, https://doi.org/10.3189/172756404781814654, 2004.

Voigt, C., Schreiner, J., Kohlmann, A., Zink, P., Mauersberger, K., Larsen, N., Deshler, T., Kro, C., Rosen, J., Adriani, A., Cairo, F., Don-

35 francesco, G. D., Viterbini, M., Ovarlez, J., Ovarlez, H., and David, C.: Nitric Acid Trihydrate (NAT) in Polar Stratospheric Clouds, Science, 290, 1756–1758, https://doi.org/10.1126/science.290.5497.1756, 2000.

von König, M., Bremer, H., Kleinböhl, A., Küllmann, H., Künzi, K. F., Goede, A. P. H., Browell, E. V., Grant, W. B., Burris, J. F., McGee, T. J., and Twigg, L.: Using gas-phase nitric acid as an indicator of PSC composition, Journal of Geophysical Research, 107, SOL 8–1–SOL 8–10, https://doi.org/10.1029/2001JD001041, 2002.

Wang, D. Y., Blom, C. E., Ward, W. E., Fischer, H., Blumenstock, T., Hase, F., Keim, C., Liu, G. Y., Mikuteit, S., Oelhaf, H., Wetzel, G.,
5   Cortesi, U., Mencaraglia, F., Bianchini, G., Redaelli, G., Pirre, M., Catoire, V., Huret, N., Vigouroux, C., Mahieu, E., Demoulin, P., Wood, S., Smale, D., Jones, N., Nakajima, H., Sugita, T., Urban, J., Murtagh, D., Boone, C. D., Bernath, P. F., Walker, K. a., Kuttippurath, J., Toon, G., Piccolo, C., Brunswick, N., Zealand, N., Science, S., and Cedex, P.: Validation of MIPAS HNO3 operational data, Atmospheric Chemistry and Physics, 7, 4905–4934, https://doi.org/10.5194/acp-7-4905-2007, 2007.

Wang, X. and Michelangeli, D. V.: A review of polar stratospheric cloud formation, China Particuology, 4, 261–271,
10   https://doi.org/10.1016/S1672-2515(07)60275-9, 2006.

Wegner, T., Grooß, J.-U., von Hobe, M., Stroh, F., Sumińska-Ebersoldt, O., Volk, C. M., Hösen, E., Mitev, V., Shur, G., and Müller, R.: Heterogeneous chlorine activation on stratospheric aerosols and clouds in the Arctic polar vortex, Atmospheric Chemistry and Physics, 12, 11 095–11 106, https://doi.org/10.5194/acp-12-11095-2012, 2012.

Wespes, C., Hurtmans, D., Clerbaux, C., Santee, M. L., Martin, R. V., and Coheur, P. F.: Global distributions of nitric acid from IASI/MetOP
15   measurements, Atmospheric Chemistry and Physics, 9, 8035–8069, https://doi.org/10.5194/acpd-9-8035-2009, 2009.

Wespes, C., Coheur, P.-F., Emmons, L. K., Hurtmans, D., Safieddine, S., Clerbaux, C., and Edwards, D. P.: Ozone variability in the troposphere and the stratosphere from the first six years of IASI observations (2008–2013), Atmospheric Chemistry and Physics Discussions, 15, 27 575–27 625, https://doi.org/10.5194/acpd-15-27575-2015, 2016.

Wohltmann, I., Lehmann, R., Rex, M., Brunner, D., and Mäder, J. A.: A process-oriented regression model for column ozone, Journal of
20   Geophysical Research, 112, 1–18, https://doi.org/10.1029/2006JD007573, 2007.

Wohltmann, I., Lehmann, R., and Rex, M.: Update of the Polar SWIFT model for polar stratospheric ozone loss (Polar SWIFT version 2), Geoscientific Model Development, 10, 2671–2689, https://doi.org/10.5194/gmd-10-2671-2017, 2017.

Atmospheric
Chemistry
and Physics
Discussions

Table 1. Proxies used for the regressions and their source

Proxy	Description	Source
SF	Solar Flux at 10.7 cm	NOAA National Center for Environmental Information
		https://www.ngdc.noaa.gov/stp/solar/flux.html
QBO	Quasi Biennial Oscillation	Free University of Berlin
	index at 10 and 30hPa	http://www.geo.fu-berlin.de/en/met/ag/strat/
		produkte/qbo/index.html
MEI	Multivariate ENSO Index	NOAA Earth System Research Laboratory
		http://www.esrl.noaa.gov/psd/data/climateindices/
VPSC	Volume of Nitric Acid Trihydrates	Dr. Ingo Wohltmann at AWI
	formed in the stratosphere	(personal communication)
AO & AAO	Arctic & Antarctic	NOAA Earth System Research Laboratory
	oscillation indices	http://www.esrl.noaa.gov/psd/data/climateindices/

Table 2. Set of variables retained by the selection algorithm for each equivalent latitude band.

70-90S	65-70S	55-65S	40-55S	30-40S	30-30	30-40N	40-55N	55-65N	65-70N	70-90N
	SF	SF	SF	SF	SF	SF	SF	SF	SF	
QBO10	QBO10	QBO10	QBO10	QBO10	QBO10	QBO10	QBO10	QBO10	QBO10	QBO10
		QBO30	QBO30	QBO30	QBO30	QBO30	QBO30	QBO30	QBO30	QBO30
COS1	COS1	COS1	COS1	COS1	COS1	COS1	COS1	COS1	COS1	COS1
SIN1	SIN1	SIN1	SIN1	SIN1	SIN1	SIN1	SIN1	SIN1	SIN1	SIN1
MEI	MEI	MEI	MEI	MEI	MEI	MEI	MEI	MEI		
VPSC	VPSC								VPSC	VPSC
	AAO	AAO	AAO	AAO	AO/AAO	AO	AO	AO		AO
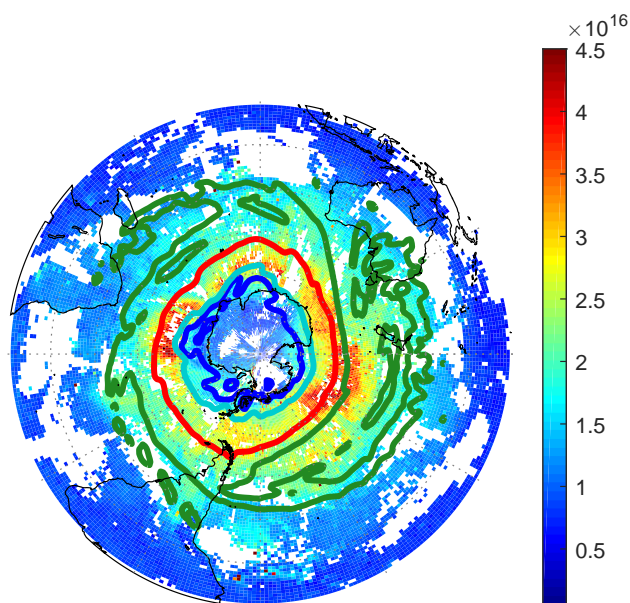
Figure 1. Example of equivalent latitude contours for -70 (blue), -65 (light blue), -55 (red) and -40 (green) equivalent latitudes. The background colors are HNO$_3$ total columns (daily mean for 21.07.2011, in molec.cm^{-2}).
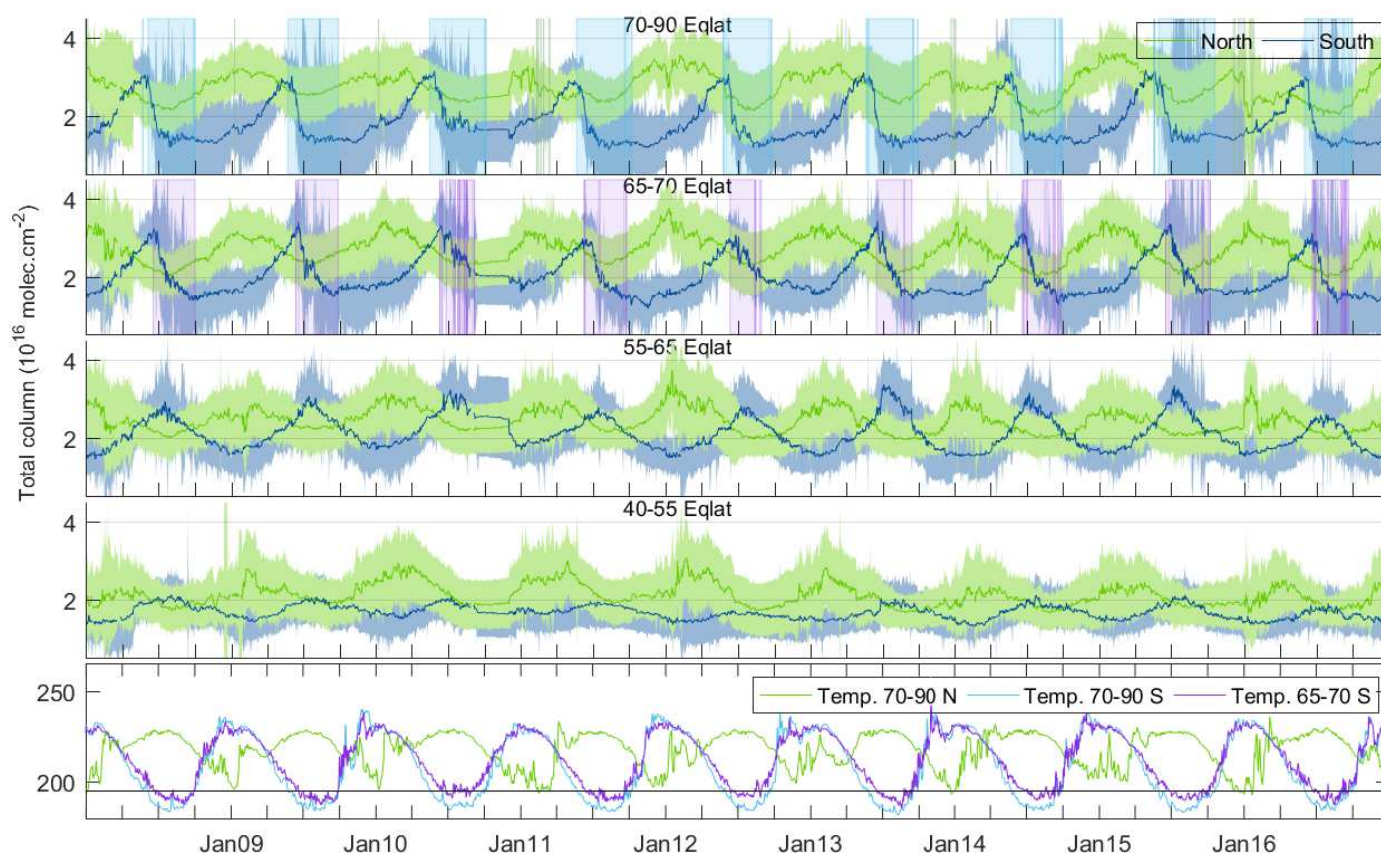
Figure 2. (four top panels) HNO$_3$ total columns time series for the years 2008-2016, for equivalent latitude bands 70-90, 65-70, 55-65 and 40-55, north (green) and south (blue). Vertical shaded areas are the periods during which the temperatures are below T_{NAT} in the north (green) and south (blue) 70-90° band, and in the south (purple) 65-70° band. (bottom panel) Temperatures time series (in K) taken at the altitude of 50 hPa for the equivalent latitude bands 70-90° North (green) and South (blue) and 65-70° South (purple). The horizontal black line represents T_{NAT}, i.e. the 195 K line.
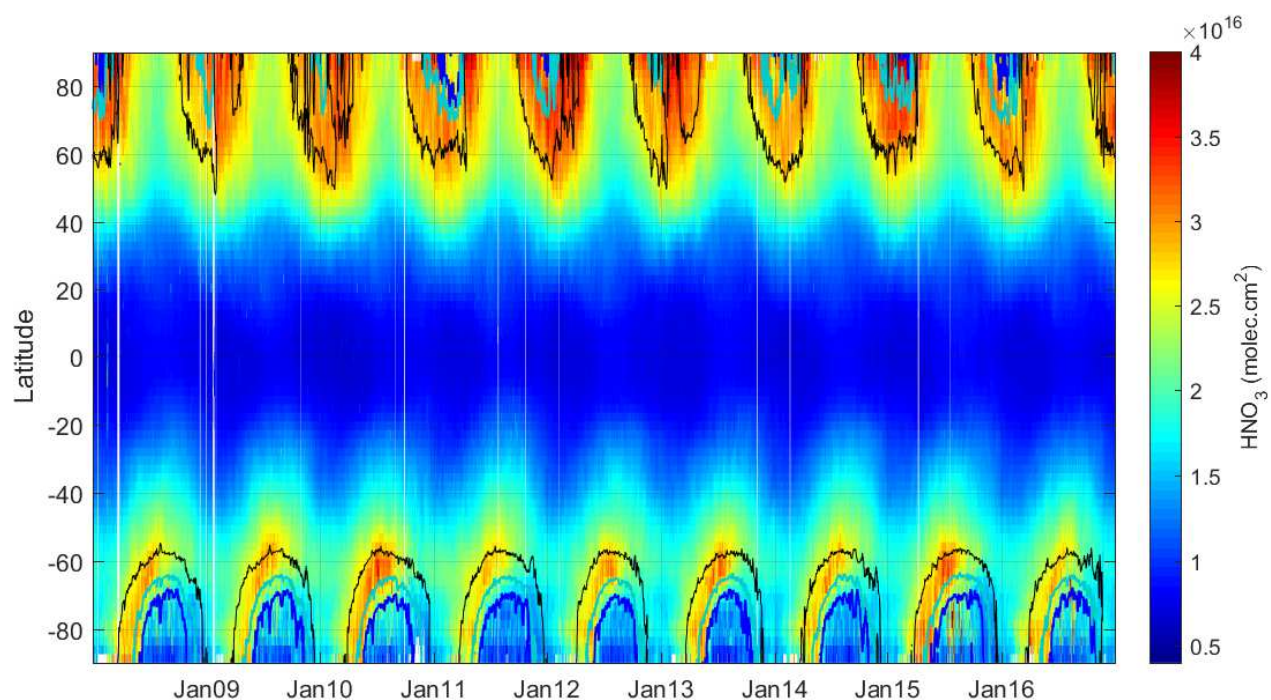
Figure 3. Zonally averaged daily HNO$_3$ total columns distribution over 2008-2016, expressed in molec.cm^{-2}. The lines represent potential vorticity contours at a potential temperature of 530 K (5 (black), 8 (cyan) and 10 (blue)×10^{-6} K.m^2.kg^{-1}.s^{-1}) which correspond to the equivalent latitudes contours illustrated in Fig 1.
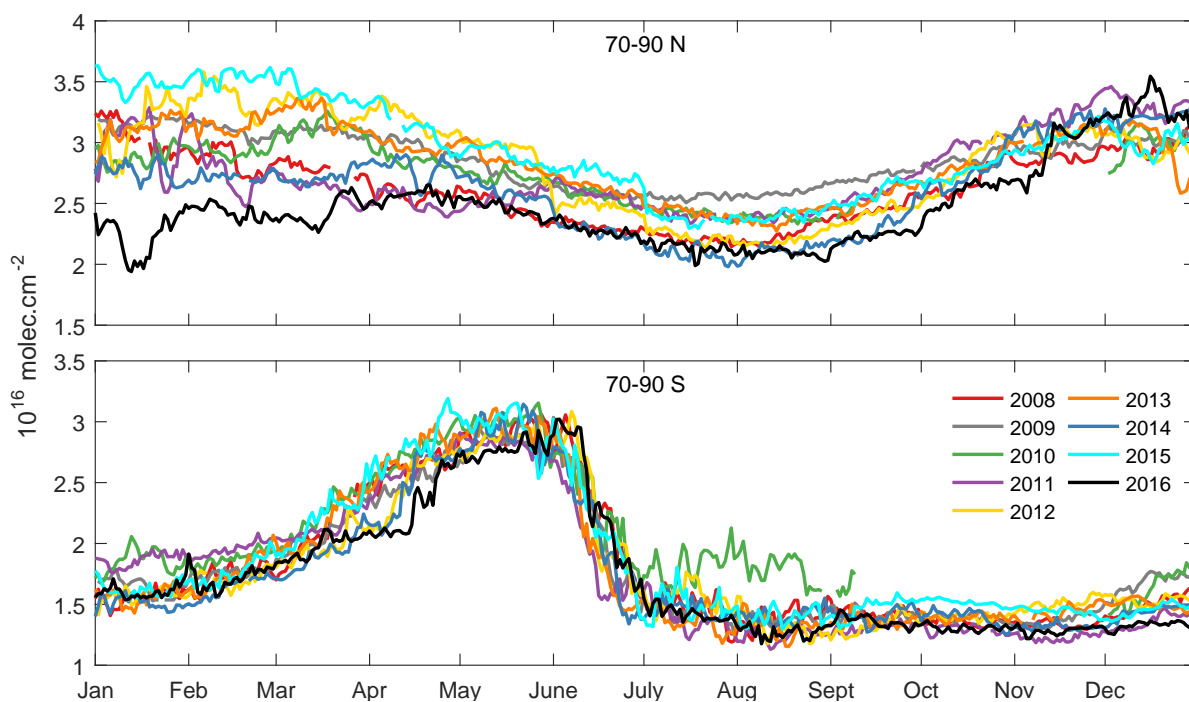
Figure 4. For northern (top) and southern (bottom) 70-90 equivalent latitude bands: HNO$_3$ total columns time series for the years 2008 to 2016 in molec.cm^{-2}. Note that the y-axis limits differ between the two plots.

Atmospheric
Chemistry
and Physics
Discussions
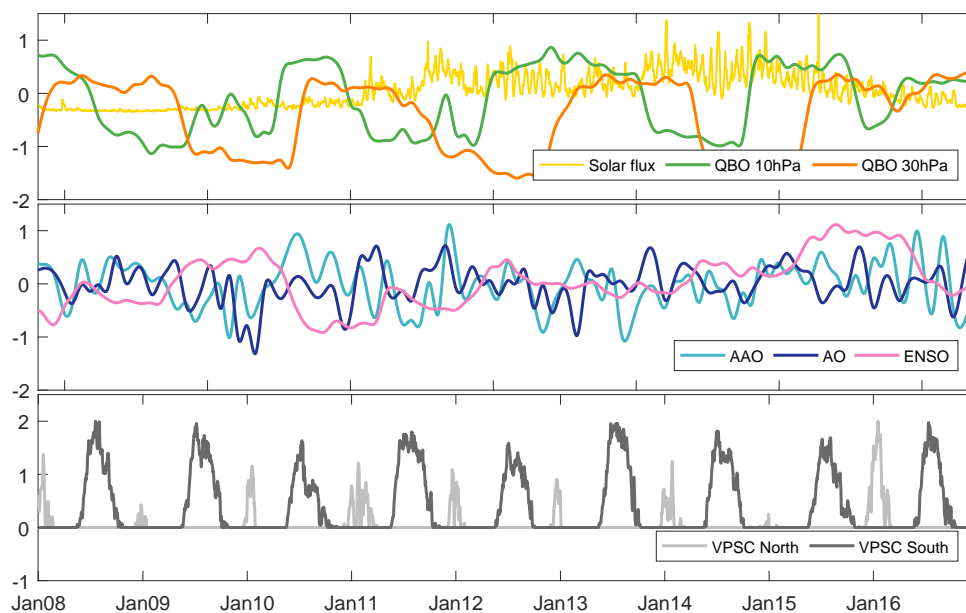
Figure 5. Normalized proxies over the IASI observations period (2008-2016). (top panel) Solar flux (yellow), QBO at 10 hPa (green) and QBO at 30 hPa (orange). (middle panel) Antarctic Oscillation (light blue), Arctic oscillation (dark blue) and Multivariate ENSO Index (MEI, pink). (bottom panel) VPSC proxy in the northern hemisphere (light grey) and in the southern hemisphere (dark grey).
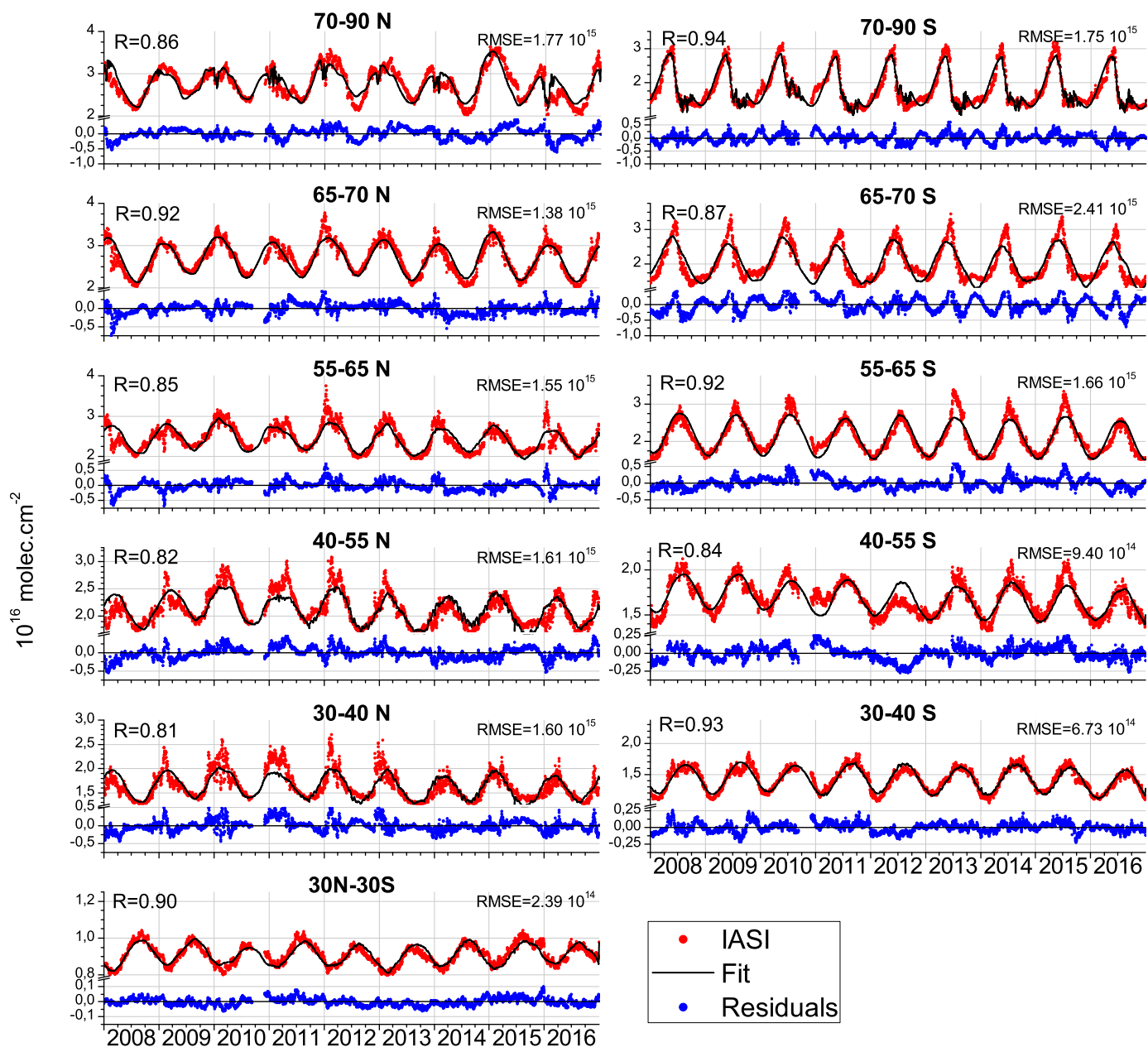
Figure 6. IASI HNO₃ total columns (red dots) for each equivalent latitude bands and the associated fitted model (black curves). The residuals are in blue, and the horizontal black line represents the zero residual line. For each equivalent latitude band, the correlation coefficient (R) between the observations and the model fit is given in the top left corner, and the root mean square error (RMSE) in the top right corner.
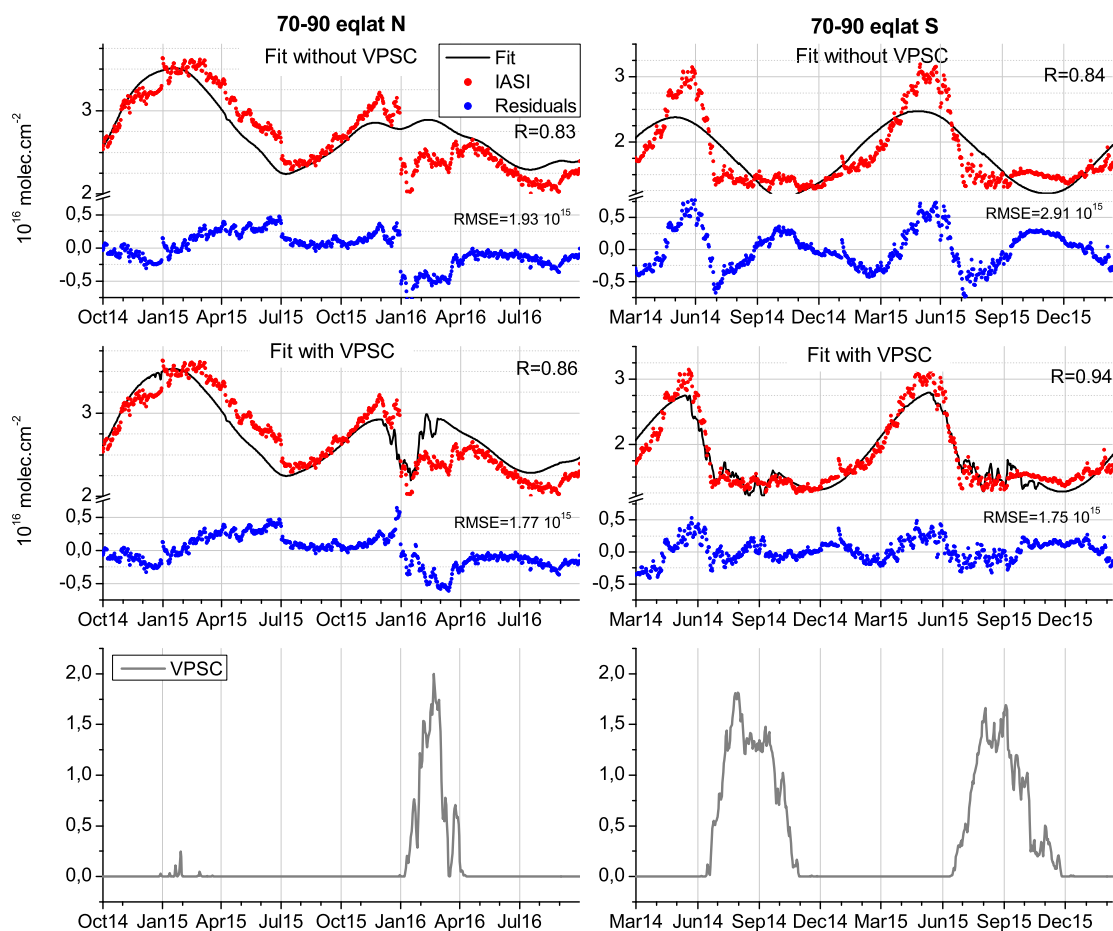
Figure 7. For north (left) and south (right) equivalent latitude bands 70-90°: (top) Total columns (in 10^{16} molec.cm^{-2}) of IASI observations (red) and the regression fit without the VPSC proxy (black), for a subset of the time series, zooming on denitrification periods. The correlation coefficients between the fit and the IASI data (R) are displayed, as well as the root mean square error (RMSE). (middle) Same as top panels but for the fit with the VPSC proxy. (bottom) Normalized VPSC proxy. Note the different time and value ranges between the two hemispheres.
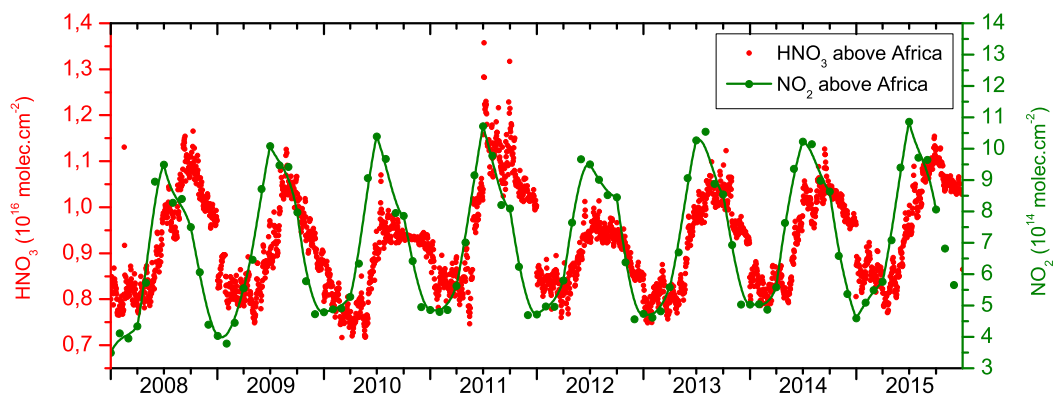
Atmospheric
Chemistry
and Physics
Discussions
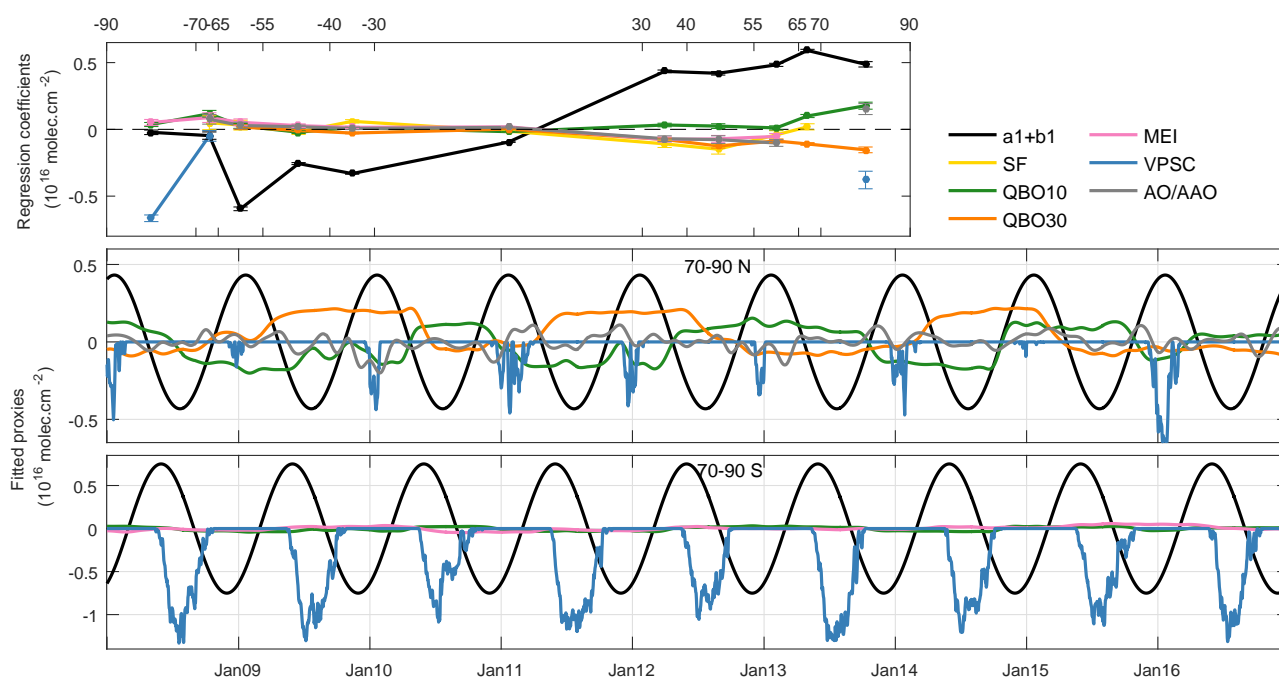
Figure 8. (top panel) Regression coefficients (x_i) and their standard error (σ_e, error bars, calculated by Eq. 3) for the selected variables in each equivalent latitude band (each data point is located in the middle of its corresponding eqlat band). (bottom panels) Fitted signal of the proxies in the eqlat bands 70-90 north (middle) and south (bottom) for the variables selected. They are calculated as [$x_i.X_i$] with X_i the normalized proxy and x_i the regression coefficient calculated by the regression model.

Atmospheric
Chemistry
and Physics
Discussions

Open Access
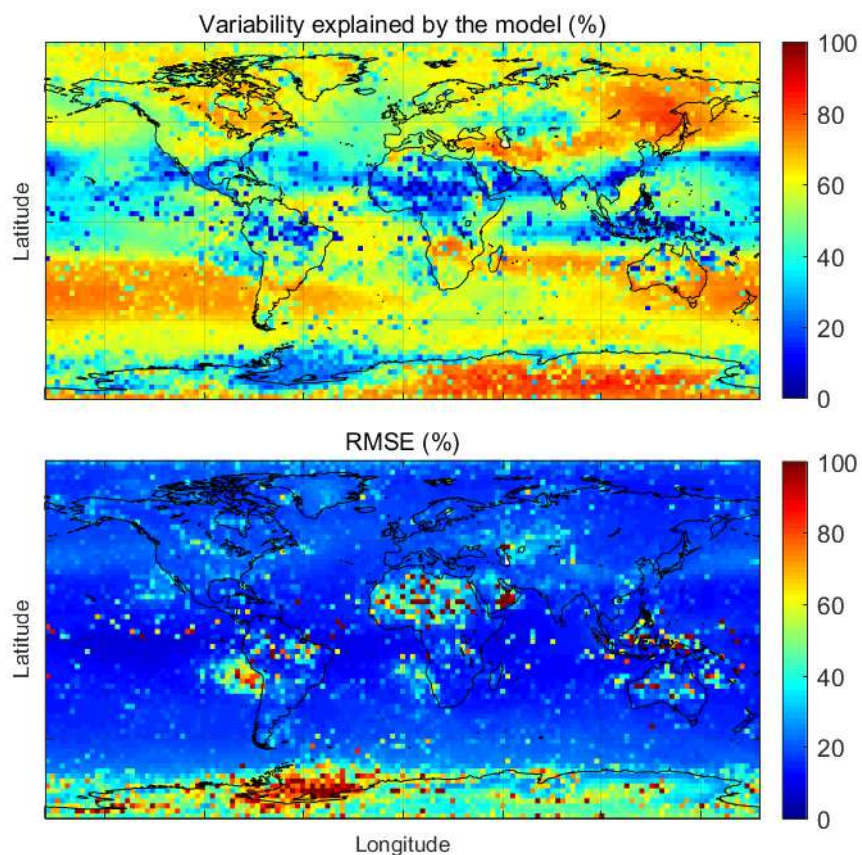

Figure 9. (top) Fraction (%) of the HNO_3 variability in the IASI observations explained by the regression model, and calculated as $[\sigma(HNO_3^{\text{fit}})/\sigma(HNO_3^{\text{IASI}}) \times 100]$. (bottom) Root Mean Square Error (RMSE) calculated for each grid cell as $[\sqrt{\frac{\sum(\text{fit-IASI})^2}{n}}]$ and expressed in %.

Figure 10. Time evolution of IASI HNO$_3$ (red) and NO$_2$ (green) from 2008 to 2015 for Africa south of the equator (5-20°S, 10-40°E). Both HNO$_3$ and NO$_2$ columns are expressed in molec.cm^{-2}. The NO$_2$ data are tropospheric columns (Valks et al., 2011) and are obtained from ftp://atmos.caf.dlr.de/. Note that the ranges differ between the two y-axes.
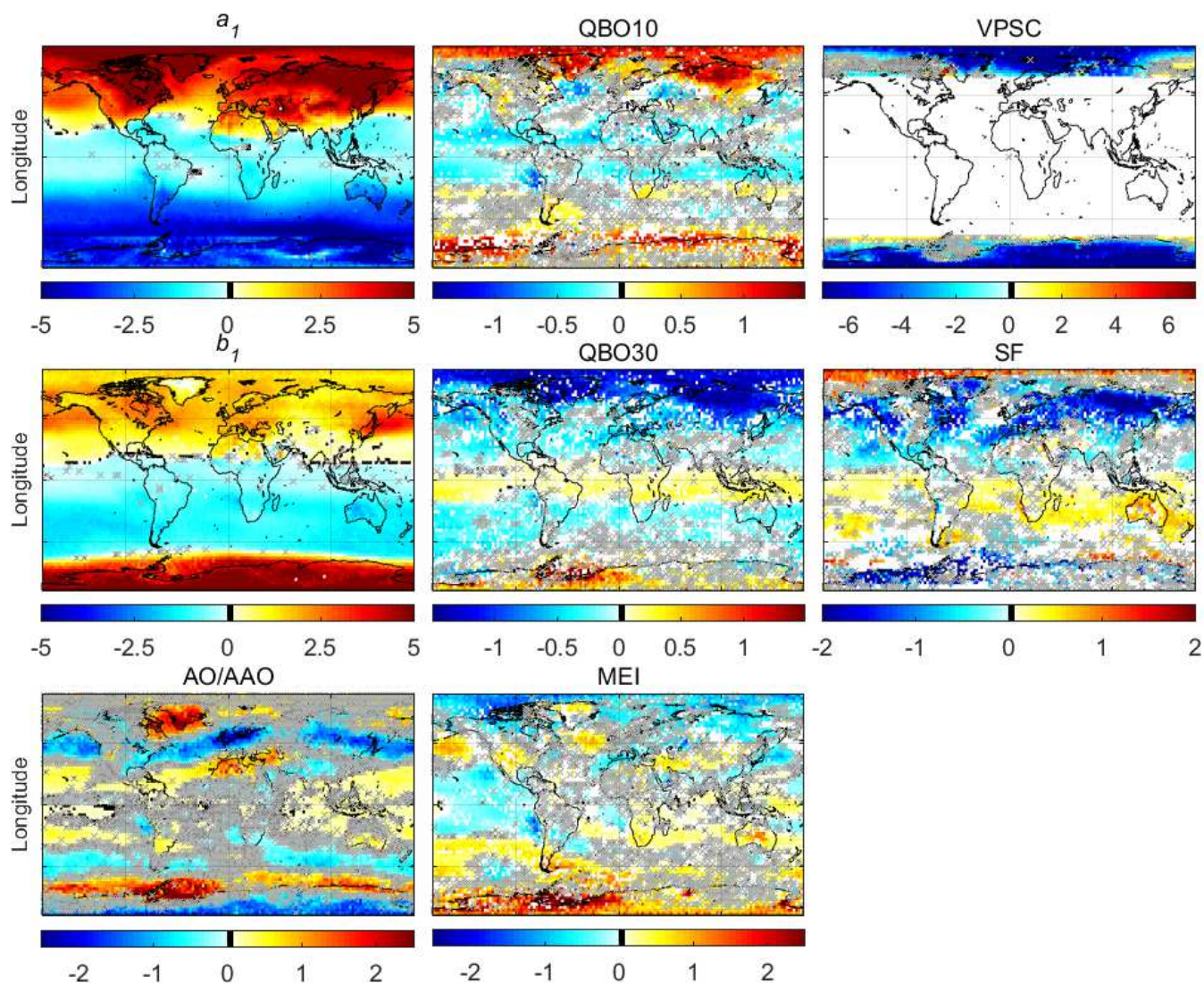
Figure 11. Global distributions ($2.5° \times 2.5°$ grid) of the regression coefficients expressed in 10^{15} molec.cm^{-2}. The gray crosses are the cells where the proxy is not significant when accounting for autocorrelation (see Eq.3). The white cells are where the proxy was not retained and the black cells represent a coefficient of 0. Note the different scales. The X axes are latitudes.